

ОБЪЕДИНЕННЫЙ  
ИНСТИТУТ  
ЯДЕРНЫХ  
ИССЛЕДОВАНИЙ

Дубна

97-118

E13-97-118

## THE $4\pi$ -FRAGMENT-SPECTROMETER FOBOS\*

The FOBOS Collaboration

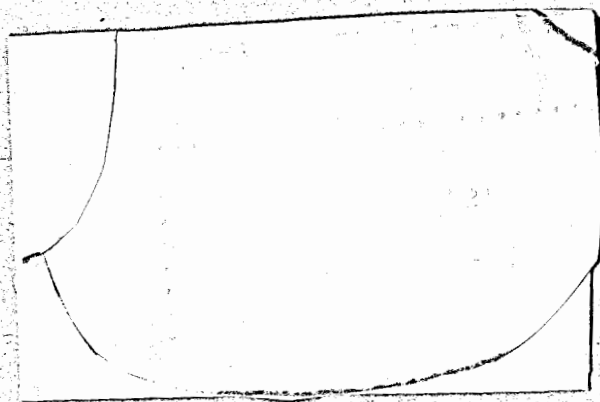
Submitted to «Nuclear Instruments and Methods in Physical Research,  
Section A»

---

\*The FOBOS project has been supported by the BMBF, Germany, contract Nr.:  
06 DR 100 and 06 DR 671

1997

W.Wagner<sup>1,2</sup>, H.G.Ortlepp<sup>1,2</sup>, C.-M.Herbach<sup>2</sup>, A.A.Aleksandrov<sup>1,4</sup>,  
I.A.Aleksandrova<sup>1,4</sup>, M.Andrassy<sup>1,2</sup>, A.Budzanowski<sup>7</sup>, B.Czech<sup>7</sup>,  
M.Danziger<sup>1,8</sup>, L.Dietterle<sup>1,2</sup>, V.N.Doronin<sup>1</sup>, S.Dshemuchadse<sup>2</sup>,  
A.S.Fomichev<sup>1</sup>, W.D.Fromm<sup>11</sup>, M.Gebhardt<sup>1,10</sup>, P.Gippner<sup>2</sup>, K.Heidel<sup>2</sup>,  
Sh.Heinitz<sup>1,2</sup>, H.Homeyer<sup>5</sup>, S.A.Ivanovsky<sup>1</sup>, D.V.Kamanin<sup>1,2</sup>,  
I.V.Kolesov<sup>1</sup>, A.Matthies<sup>1,2</sup>, D.May<sup>1,2</sup>, S.I.Merzlyakov<sup>1</sup>, W. von Oertzen<sup>6</sup>,  
Yu.Ts.Oganessian<sup>1</sup>, G.Pausch<sup>2</sup>, Yu.E.Penionzhkevich<sup>1</sup>, Yu.V.Pyatkov<sup>4</sup>,  
S.V.Radnev<sup>3</sup>, G.Renz<sup>1,2</sup>, L.A.Rubinskaya<sup>1</sup>, I.D.Sandrev<sup>3</sup>, K.D.Schilling<sup>2</sup>,  
W.Seidel<sup>2</sup>, D.I.Shishkin<sup>1</sup>, A.P.Sirotnin<sup>1</sup>, H.Sodan<sup>11</sup>, O.V.Strekalovsky<sup>1</sup>,  
V.G.Tishchenko<sup>1</sup>, V.V.Trofimov<sup>1</sup>, I.P.Tsurin<sup>1</sup>, C.Umlauf<sup>1,2</sup>,  
D.V.Vakatov<sup>1</sup>, V.M.Vasko<sup>1</sup>, V.A.Vitenko<sup>9</sup>, E.Will<sup>2</sup>, M.Wilpert<sup>6</sup>,  
V.E.Zhuchko<sup>1</sup>, P.Ziem<sup>5</sup>, L.Zrodowski<sup>7</sup>



<sup>1</sup>Joint Institute for Nuclear Research, 141980 Dubna (Moscow Region), Russia

<sup>2</sup>Forschungszentrum Rossendorf e.V., 01314 Dresden, PO Box 510119, Germany

<sup>3</sup>Laboratory for Technical Developments and Applications, Bulgarian Academy of Sciences, 1184 Sofia, Bulvar Zarigradsko Chosse 72, Bulgaria

<sup>4</sup>Moscow Engineering Physics Institute, 115409 Moscow, Kachirskoye Chosse 31, Russia

<sup>5</sup>Hahn-Meitner-Institut GmbH, 14195 Berlin, Glienicke Str.100, Germany

<sup>6</sup>Freie Universität Berlin, 14195 Berlin, Arnimallee 14, Germany

<sup>7</sup>Henryk Niewodniczansky Institute of Nuclear Physics, 31-342 Cracow, ul.Radzikowskiego 152, Poland

<sup>8</sup>Technische Universität Dresden, 01062 Dresden, Mommsenstr.13, Germany

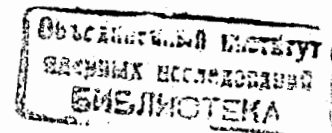
<sup>9</sup>Khlopin-Radium-Institute, St.Petersburg, ul.Rentgen'a 1, Russia

<sup>10</sup>Johann Wolfgang Goethe - Universität, 60054 Frankfurt am Main, PO Box 111932, Germany

<sup>11</sup>Zentralinstitut für Kernforschung (before 1992), Rossendorf, Germany

THE  $4\pi$ -FRAGMENT-SPECTROMETER FOBOS

The FOBOS Collaboration



## Contents

1. Introduction
2. FOBOS set-up
  - 2.1 Mechanical design
  - 2.2 Position-sensitive avalanche counters
  - 2.3 Axial ionization chambers
  - 2.4 Evacuation and gas-supply system
  - 2.5 Scintillator shell
  - 2.6 Forward array
3. Data acquisition system
  - 3.1 First-level trigger
  - 3.2 Read-out electronics
  - 3.3 Experimental data structure
  - 3.4 Data analysis software
4. Calibration procedures
  - 4.1 Parameter calibration for the gas-filled detector modules
    - 4.1.1 *Coordinates calibration of the position-sensitive avalanche counters*
    - 4.1.2 *Energy calibration of the Bragg chambers*
    - 4.1.3 *Time calibration of the position-sensitive avalanche counters*
  - 4.2 Calibration of the scintillation detectors
5. Physical observables of charged particles
6. Experiments at FOBOS
  - 6.1 Fragment spectroscopy of spontaneous fission
  - 6.2 Fragmentation of hot nuclei
    - 6.2.1 *TKE - M distributions of binary fission of hot nuclei*
    - 6.2.2 *Velocity analysis of ternary decays*
    - 6.2.3 *The charged-particle clock*
7. Summary

## Acknowledgments

## Tables

## References

## 1. INTRODUCTION

The  $4\pi$ -fragment-spectrometer FOBOS [1,2], proposed for the first time in 1984 [3] with the aim to study heavy-ion induced reactions in the low and intermediate energy region of  $10 \div 100$  AMeV, has been built at the Flerov Laboratory of Nuclear Reactions of the Joint Institute for Nuclear Research in Dubna. It is now regularly operating in its full configuration for nuclear physics research.

At that time planned for working at the beams of a proposed cyclotron-tandem facility [4], FOBOS is presently supplied by heavy-ion beams of the isocronos cyclotron U-400M which has recently been equipped with an ECR ion-source [5]. For ions up to about Xe this arrangement provides nearly the same beam energies as those expected from the cyclotron-tandem [6]. By means of projectile fragmentation, radioactive secondary-ion beams became possible. This opens a new perspective for heavy-ion research in the mentioned energy region.

The spectrometer FOBOS has been designed for reaction studies in direct kinematics, i.e., a light projectile impinges upon a heavy target nucleus. Since at bombarding energies higher than about 20 AMeV, the complete fusion scenario changes over to an incomplete fusion mechanism, the linear momentum (LMT) transferred to the compound-like composite system stays relatively moderate. Depending on its mass and excitation energy ( $E^*$ ), the particle decay of this system is mostly characterized by the emission of  $1 \div 3$  heavy fragments (e.g. fission fragments (FF) or heavy residues (HR)), a small number of fragments of intermediate mass (IMF), conventionally defined as being located between  $\alpha$ -particles and FF, a fairly large number ( $\approx 10 \div 30$ ) of neutrons and a medium number of light charged particles (LCP). FOBOS is able to register *charged* reaction products only, from protons up to HR. Due to reaction kinematics, most of the ejectiles are directed into the entire solid angle ( $\Delta\Omega$ ). Therefore, the basic geometry of the detector set-up was chosen to be that of a sphere surrounding the target. The mechanical design represents a 32 face truncated isocahedron consisting of 20 regular hexagons and 12 regular pentagons.

The intention to perform exclusive spectroscopy of charged fragments within a broad dynamic range, covering large intervals of atomic number ( $Z$ ), mass number ( $A$ ), and simultaneously a considerable part of solid angle  $4\pi$  as well, requires some reasonable compromise between registration efficiency, detector granularity, detection thresholds, possible counting rates etc.. For this purpose, the so-called *logarithmic detection principle* has been applied. This principle consists of a combination of different types of detectors (mainly gas-

filled and solid state detectors), so that a successive increase of the stopping power on the flight path of the particles is accomplished. The consequence is often a rather heterogeneous construction of the spectrometer, which for technical reasons seldom allows for a geometrical efficiency of actually  $4\pi$ .

The spectrometer FOBOS consists of three consecutive shells of particle detectors and a more granular forward array. A relatively long flight path of 50 cm between the target and the inner detector shell of position-sensitive avalanche counters (PSAC) is available for a precise time-of-flight (TOF) and coordinates ( $\vartheta, \phi$ ) measurement of fragments with  $Z > 2$ . By utilizing the TOF and the pulse-height ( $\Delta E$ ) information of the PSAC, a rough Z-identification is possible for heavy species not reaching the next detector shell, e.g. evaporation residues (HR).

The second detector shell consists of 30 axial Bragg ionization chambers (BIC) which register the full energy-loss distribution (Bragg-curve) of the fragments stopped within the gas-volume. The residual fragment energy ( $E_R$ ) and the magnitude of the Bragg-peak (BP), being a measure of Z, are directly derived. From the TOF- and the  $E_R$ -information the masses ( $m_i$ ) of the fragments can be calculated applying a suitable correction procedure which takes into account the different energy losses in all the detector materials penetrated. Hence, the momentum vectors ( $p_i$ ) can be derived independently for each fragment (i) "event by event". This feature is a necessary condition for an exclusive measurement.

Since the PSAC and BIC are not sensitive to low-ionizing LCP ( $Z = 1 + 2$ ) a third, more granular, scintillator shell of CsI(Tl)-detectors [7] is arranged behind them. The LCP are analyzed by their signal pulse-height and -shape. Fast LCP do not affect the registration of fragments in the PSAC and BIC. Therefore, the correlations between fragments and LCP can be studied for all possible relative angles. Furthermore, the well known  $\Delta E$ -E-method can be applied for the identification of high-energetic IMF which penetrated the BIC and are stopped in the scintillators.

In each case, one PSAC, one BIC, and a mosaic of 7 CsI(Tl) scintillation counters are arranged in altogether 30 separate detector-modules [8] which are mounted to the central vacuum chamber from outside. The parameters of a particle, measured or derived from the signals delivered by a FOBOS module, are schematically drawn in fig. 1.

Two of the pentagons of the main geometrical construction are used for the beam entrance and exit. A more granular concentric array of phoswich detectors (see chapter 2.6) is placed inside the central vacuum chamber covering forward angles of  $\vartheta = 4.5^\circ \pm 26^\circ$ .

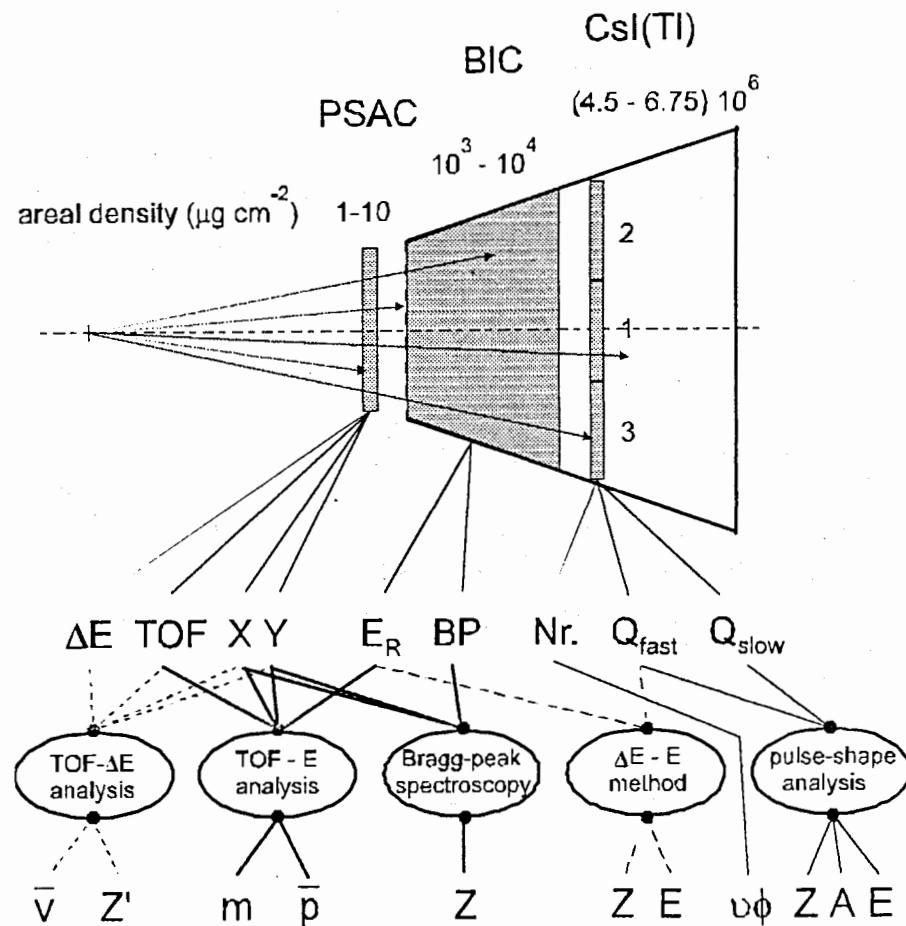


Fig. 1 Parameters of charged particles, measured or derived from the signals delivered by a detector module. Different methods of analysis are applied, if  
 (i) only the PSAC has fired (dotted lines), (ii) the PSAC and BIC have fired (thick full lines),  
 (iii) only a CsI(Tl)-detector (1,2,3, ... 7) has fired (thin full lines), and  
 (vi) the BIC and a CsI(Tl)-detector have fired (dashed lines).  
 The logarithmically increasing stopping power of the different detector shells is illustrated by the given mean areal densities of the detector materials of the PSAC, BIC, and CsI(Tl)-crystals for typical experimental conditions.

In the following chapters, main elements of the  $4\pi$ -fragment-spectrometer FOBOS are described paying more attention to original and advantageous features than to the basic detection principles which are widely known from the literature. A general comparison with other  $4\pi$ -devices is knowingly omitted, since every serious and detailed inspection of the detector capabilities rather demonstrates their complementary properties in nuclear research than any supersession. Some results obtained in the first series of experiments during the period of commissioning of this new spectrometer are mainly given for illustration of its properties.

It has to be mentioned, that a similar  $4\pi$ -array for charged fragments has been built at the Cyclotron Laboratory of the Michigan State University, East Lansing, USA [9]. The concept of the spectrometer FOBOS resembles it in general design, and several detection principles applied at this two devices are almost identical. Nevertheless, important properties and detector parameters of FOBOS could be reached due to the considerable amount of completely different technical solutions, in particular, due to the three times longer flight path.

## 2. FOBOS SET-UP

### 2.1 Mechanical design

The general lay-out of the spectrometer FOBOS is schematically shown in fig. 2. The central vacuum chamber [10] is a monolithic hollow body with an inner diameter of 1330 mm. From outside the basic shape is that of a precisely manufactured ( $\pm 0.2$  mm) 32-face truncated isocahedron with circular holes in the centers of the hexagonal ( $\varnothing = 480$  mm) and pentagonal ( $\varnothing = 380$  mm) surface elements for mounting the 20 large and 10 small detector modules, respectively. The angles ( $\vartheta, \phi$ ) of the centers of the modules are given in tab. 1.

The entrance tube to FOBOS has an inner diameter of 300 mm. A cone of  $\vartheta \approx 12^\circ$  at the beam exit can house a special forward array. Two carrier columns support the detector axis at both sides. The evacuation of the central volume is performed along the main axis. The vacuum connections to the beam line allow to rotate the fully mounted FOBOS device for changing the modules and for other services.

The hexagonal- and pentagonal-shaped frames of the PSAC are mounted separately in front of the BIC entrance windows. Part of the mechanical structure of the BIC protrudes into the central vacuum chamber. The PSAC of the first detector shell also form a truncated isocahedron-like shape at a distance of  $\approx 50$  cm from the target (fig. 2). Their sensitive areas are circles of  $\varnothing = 327$  mm and  $\varnothing = 243$  mm at the large and small detector modules, respectively.

The conical shaped BIC have apertures of 260.0 msr ( $\Delta\vartheta = 33.08^\circ$ ) and 167.8 msr ( $\Delta\vartheta = 26.54^\circ$ ), respectively. This results in a total solid angle of 7.1 sr (56.5 % of  $4\pi$ ) covered by the PSAC, and 6.88 sr (54.7 % of  $4\pi$ ) covered by the BIC.

The mosaics of 7 hexagonal-shaped CsI(Tl)-crystals are positioned together with their light-guides and photomultipliers inside the BIC cases covering 84 % of the BIC aperture. Rubber rings pressed to the phototubes serve as seals between the gas-volumes of the BIC and the atmosphere.

The forward array of 92 phoswich detectors arranged in 6 concentric rings around the beam axis at distances of  $10 \div 25$  cm from the target covers the interval of polar angles of  $\vartheta = 4.5^\circ \div 26.5^\circ$ . It can be inserted into the central vacuum chamber through the exit cone. The outer ring of the forward array slightly overlaps with the BIC positioned in forward direction at  $\langle \vartheta \rangle = 37.4^\circ$ .

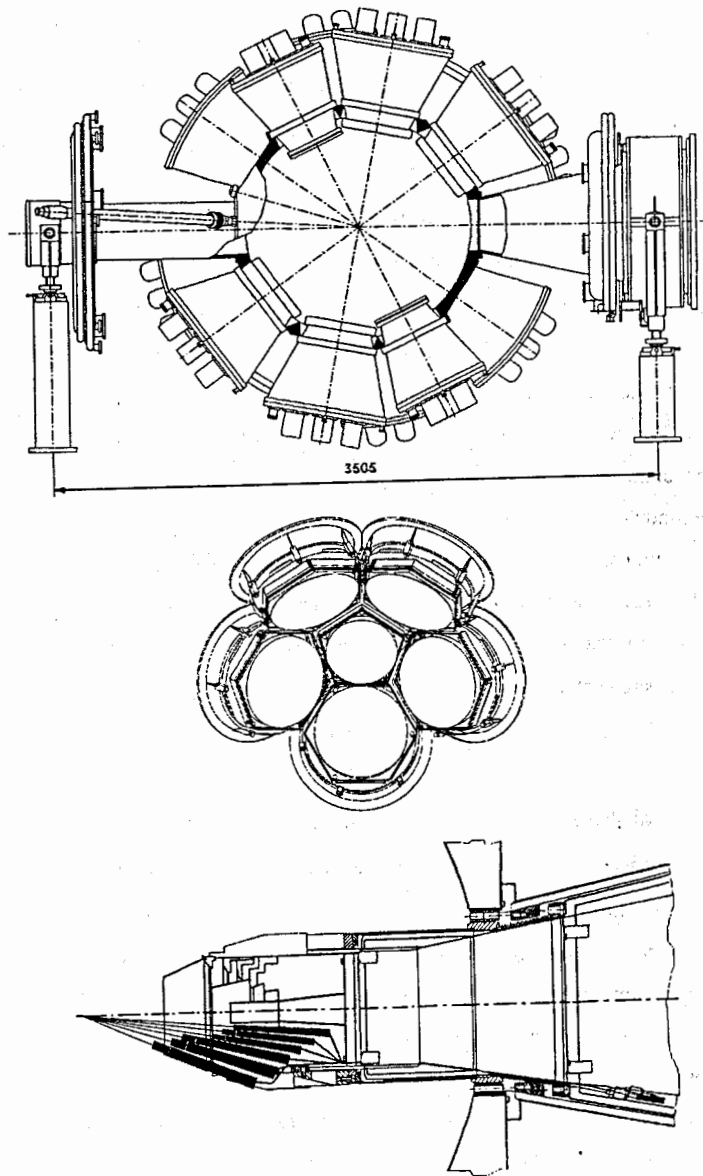


Fig. 2

Fig. 2 General lay-out of the FOBOS spectrometer. Cross-sectional view of the central vacuum chamber with mounted detector modules (upper part). The beam enters from the left side. The exit cone at the right side houses the forward array. A cross-sectional view of the forward array is shown in the lower part. (For more clearness only half of the phoswich detectors are drawn.) The mechanical arrangement of five large hexagonal PSAC surrounding one small pentagonal PSAC is shown in the central part. The circles define the sensitive areas of the PSAC.

## 2.2 Position - sensitive avalanche counters

The PSAC are based on the principles described in ref. [11]. Three thin Mylar foils ( $1.2 \mu\text{m}$ ) are used as cathode and PSAC windows. The central cathode-foil is covered by  $40 \mu\text{g cm}^{-2}$  thick Au layers. It delivers the timing signal. Two perpendicular wire-planes (made of  $30 \mu\text{m}$  thick Au-plated W, spaced by 1 mm) are positioned at both sides from the common cathode at a distance of  $3 \text{ mm} \pm 50 \mu\text{m}$ . They serve as anode coordinate grids. The window foils are glued to special frames which can be changed individually in the case of leakage. The transparency of the PSAC amounts to 92 %.

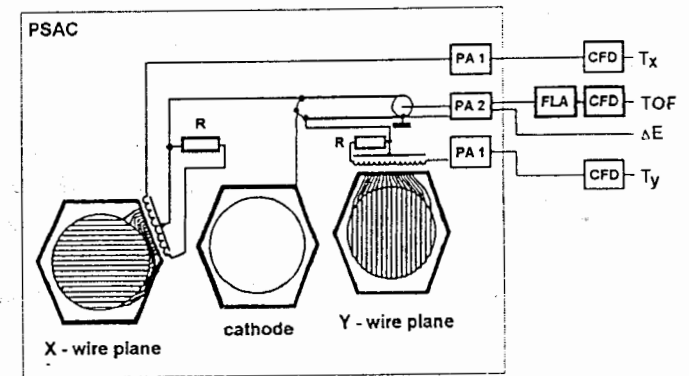


Fig. 3 Principal scheme of the PSAC read-out. Delay lines are capacitively coupled to the X- and Y-wire planes. Three preamplifiers (PA) for the coordinates and timing signals are directly mounted to the PSAC frame. A fast linear amplifier (FLA) for the timing signal (TOF) drives the long cable line to the front-end electronics in the measurement hall. A CAMAC module contains the three constant fraction discriminators (CFD).

Pairs of neighboring coordinate wires are connected with conductive strips which are capacitively coupled to a wound read-out delay-line of  $1.4 \text{ ns mm}^{-1}$  specific delay and  $560 \Omega$  impedance. The two delay lines of the coordinate grids are matched with resistors at one end and coupled to special read-out amplifiers at the other end. The cathode read-out circuit delivers an amplified current signal for timing and a charge signal for pulse-height analysis. All electronic channels are protected against damage in the case of spark discharges in the counters. The surface-mounted circuits and the delay lines are placed at nonsensitive areas directly inside the PSAC frames. The spatial resolution of the PSAC amounts to  $\Delta x = \Delta y \approx 1.5 \text{ mm}$ . A principal scheme of the PSAC read-out is shown in fig. 3.

The counter-gas is pentane at a pressure between 200 Pa and 800 Pa. The voltage (typically  $\approx 500 \text{ V}$ ) is set about 5 V below the onset of spark discharges induced by feed-back effects after passing of the highly ionizing particles. This voltage level guarantees an effective registration of heavy fragments with a lower threshold of  $\approx 0.05 \text{ AMeV}$ . The efficiency of registration drops for  $\alpha$ -particles at energies of  $\geq 1.5 \text{ AMeV}$  because of the decreasing energy loss in the sensitive volume.

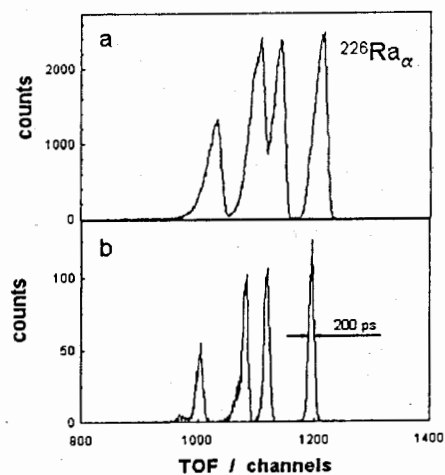


Fig. 4 Time-of-flight spectrum of a  $^{226}\text{Ra}$   $\alpha$ -source measured by a PSAC against the timing reference signal of a small transmission avalanche counter. The energies of the  $\alpha$ -lines are given in fig. 12.

(a: irradiating the entire sensitive area, b: irradiating only a small central part of the PSAC) The time resolution is 200 ps.

Using a  $^{226}\text{Ra}$   $\alpha$ -source, the time resolution of the PSAC has been measured against a small parallel-plate avalanche counter which provided the START-signal for the TOF measurement. Fig. 4b represents a TOF spectrum where only a small

central area of the counter was irradiated. Typically, the FWHM amounts to  $\approx 200 \text{ ps}$ . Irradiating the whole sensitive area of the PSAC (fig. 4a), the resolution becomes worse by a factor of about three. This is due to the influence of electronic signal delays. Therefore, a map of calibrated TOF signals was created for each PSAC (fig. 5) which can be used for a coordinate-dependent correction of the measured TOF. This procedure allows to define the TOF of the fragments with an accuracy of  $\approx 100 \text{ ps}$ .

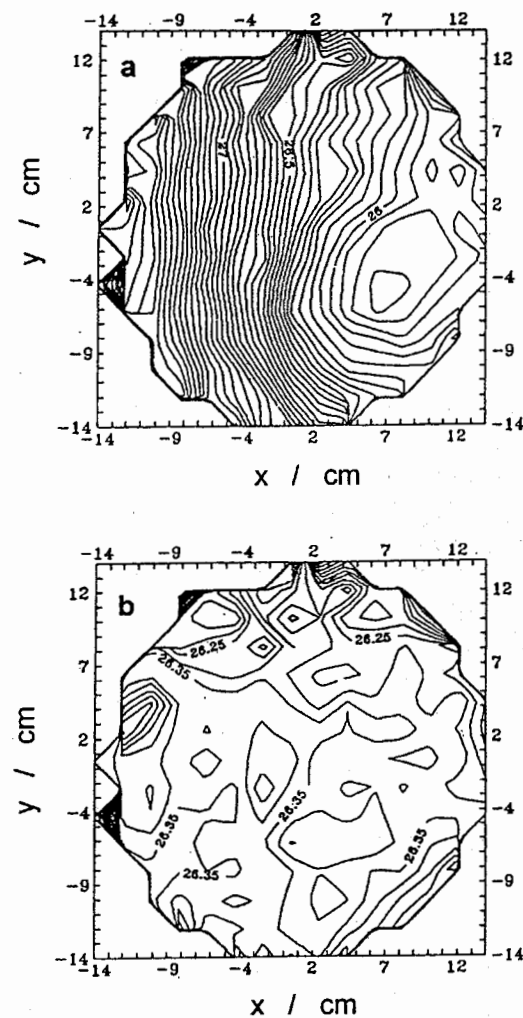


Fig. 5 Contour plots of calibrated time-of-flight signals of a PSAC with a step of 0.05 ns. (a: uncorrected; b: corrected for the dependence on the PSAC coordinates)

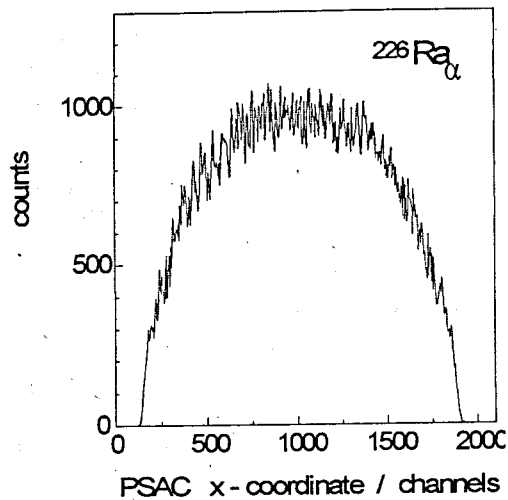


Fig. 6 Coordinate spectrum of a PSAC measured using a  $^{226}\text{Ra}$   $\alpha$ -source.

A typical coordinate spectrum measured with a  $^{226}\text{Ra}$   $\alpha$ -source is shown in fig. 6. The shape corresponds to the aperture defined by the PSAC against the point-like source. The image of the supporting structure of the window foil of the BIC can be seen in the coordinates scatterplot of fig. 7.

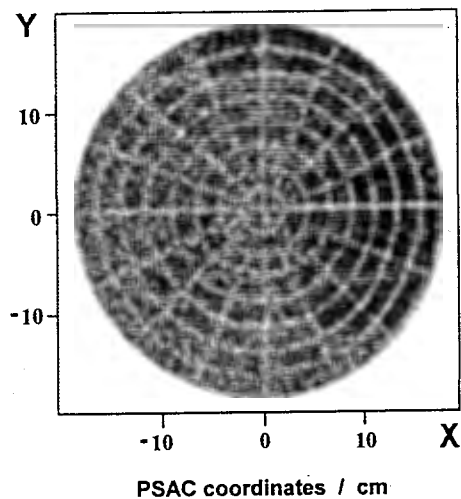


Fig. 7 Shadow zone in the coordinates scatterplot of a PSAC imaging the supporting structure of the window foil of the BIC. The plot is generated by correlated events in the PSAC and the BIC positioned behind it.

A rough selection of heavy fragments by its mass can be carried out using the  $\Delta E$  versus TOF scatterplot of the PSAC (fig. 8). The  $E_R$  versus TOF scatterplot (fig. 9) delivers information about correlated and random events necessary in the case of a pulsed micro-structure of the ion beam. In most cases a deflecting high voltage at the target can not be applied due to the residual pressure inside the central vacuum chamber mainly caused by the diffusion rate of the

working gas of the BIC through the thin window foils. Therefore, a considerable high  $\delta$ -electron background ( $\approx 10^7 \div 10^8 \text{ s}^{-1}$ ) correlated with the beam bunches has to be handled by the PSAC electronics.

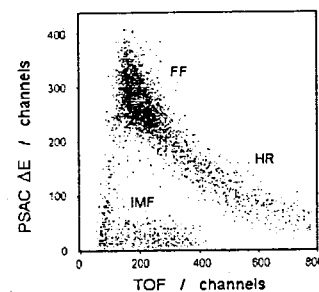


Fig. 8  $\Delta E$  versus TOF scatterplot measured by a PSAC for the reaction  $^{14}\text{N}$  (53 AMeV) +  $^{197}\text{Au}$ . (FF - fission fragments, HR - heavy residues, IMF - intermediate mass fragments)

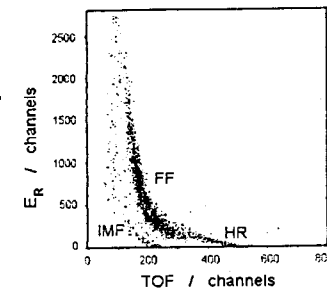


Fig. 9  $E_R$  versus TOF scatterplot measured by a gas-detector module for the reaction  $^{14}\text{N}$  (53 AMeV) +  $^{197}\text{Au}$ . (Note that the time interval of the registration of heavy residues is considerably shorter than in the case shown in fig. 8.)

Two advantages of the detector concept of FOBOS should be emphasized :

- (i) The long flight path and the timing properties of the PSAC make it possible to apply the TOF- $E_R$ -method for the mass determination of the fragments instead of the  $\Delta E$ - $E$ -method which has its natural energy limits caused by the  $\Delta E$ -detector. In other systems often heavy fragments (FF, HR) can not be identified (e.g. at the  $4\pi$ -array INDRA [12] where small ionization chambers deliver the  $\Delta E$ -information, but timing can not be used, or at the MSU  $4\pi$ -array [9] where the compact detector design required more thick entrance windows of the BIC leading to considerably high registration thresholds).
- (ii) The excellent spatial resolution of the PSAC together with the mentioned principle of mass determination allows for a more precise determination of the linear momenta of the fragments.



### 2.3 Axial ionization chambers

The principle of a BIC was first described in ref. [13]. Since the electric field is parallel to the direction of the incoming particles, the registered pulse-shape of a fragment stopped in the gas-volume of the BIC represents an image of the specific energy loss on the ionization path, which is characterized by the Bragg-curve. The integral of the electronic charge created is proportional to the energy ( $E_R$ ) of the fragment, and the maximum of the ionization-density distribution of the fragment in its stopping path (BP) is a smooth function of  $Z$  (see also chapter 4.1.2).

A sketch of the lay-out of the detector module is shown in fig. 10.

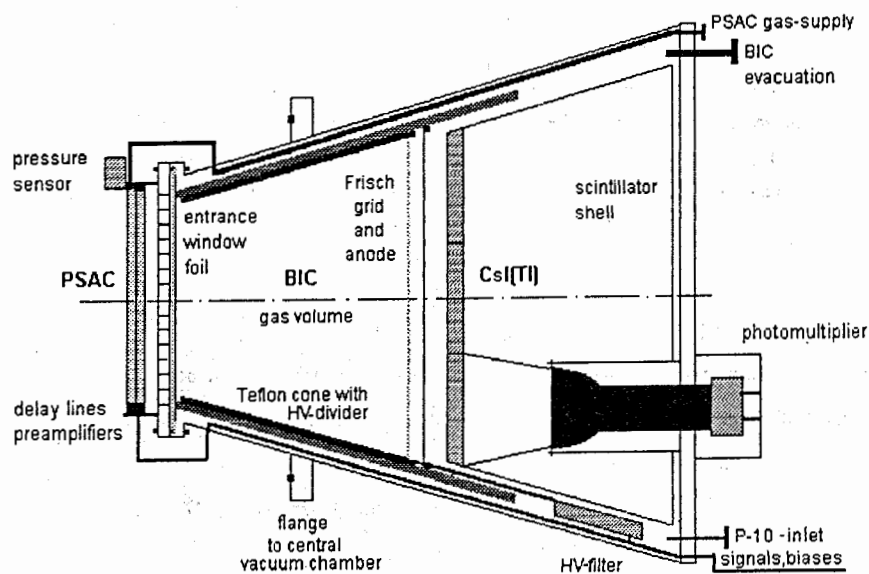


Fig. 10 Sketch of the general lay-out of a detector module.

The entrance windows of the large and small BIC, made of  $1.5 \div 3 \mu\text{m}$  thick aluminized Mylar, are of  $\varnothing 385 \text{ mm}$  and  $\varnothing 285 \text{ mm}$ , respectively. The sensitive depth of the BIC is 250 mm. To withstand the pressure of the working gas, the delicate window foil, which at the same time serves as cathode, has to be supported by a twofold structure — a heavy

carrier of a transparency of 94 % and an adjacent etched Ni-mesh having a cell dimension of  $\varnothing 2.7 \text{ mm}$ . Cells smaller than  $\varnothing 3 \text{ mm}$  are necessary, because, otherwise, the extremely thin foils would not hold gas pressures up to 100 kPa needed to stop most of the IMF within the sensitive depth. This mesh, however, reduces the transparency of the entrance window to only 75 %, causing the most serious restriction with respect to the effective solid angle of the spectrometer.

Together, the PSAC foils and the BIC window foil create a dead layer for fragment spectroscopy of  $\approx 510 \mu\text{g cm}^{-2}$ . The residual energy threshold for FF of  $\approx 0.3 \text{ AMeV}$  is lower by a factor of  $\approx 4$  compared with the MSU  $4\pi$ -array [9], while the effective solid angle is smaller by a factor of  $\leq 2$ . For the registration of FF, having typical c.m. energies of  $0.5 \div 1.5 \text{ AMeV}$ , this seems to be a good compromise.

The shaping of the axial electric field is performed by 5 mm spaced Cu-strips coated on the inner side of the conical Teflon insulator. The voltage divider provides equal potential steps. The advantage of using a homogeneous field, also in a BIC with a large aperture, was already demonstrated in ref. [14].

The Frisch grid is placed 10 mm in front of the anode. It consists of two perpendicular wire-planes ( $50 \mu\text{m}$  thick Cu-Be spaced by 1 mm). The anode is a  $10 \mu\text{m}$  thick aluminized Mylar foil. The positive voltage is fed via a passive filter and attenuator to the anode and the Frisch grid to achieve optimum field strength relations [15]. In typical experiments the BIC are filled with a P-10 gas-mixture (90 % Ar + 10 %  $\text{CH}_4$ ) at a pressure of  $20 \div 40 \text{ kPa}$  and operated with an anode voltage of  $1.5 \div 3 \text{ kV}$ . At the design limit of 100 kPa this voltage reaches 8 kV.

Conventionally, the charge signal is split and shaped by two different time constants to deduce the  $E_R$ - and  $Z$ -information of a BIC. In our case, the long electron drift-time (up to  $4 \mu\text{s}$ ) would cause a considerably large ballistic deficit. Therefore, a new processing method has been developed which derives the  $E_R$ - and BP-signals directly from digitized signal samples. The electronic set-up of this method has been published earlier [16], its principle is shown in fig. 11. The read-out system consists of a charge-sensitive preamplifier, a Bragg-curve digitizer (BCD) and a digital processor (BDP). The BIC-signal is shaped by a short time constant ( $\tau = 0.2$  or  $0.4 \mu\text{s}$ ) in a spectroscopic amplifier and further digitized by an 8-bit flash ADC with a quartz-stabilized sampling frequency of 10 MHz. When a signal is recognized by the threshold comparator, two arithmetic units are activated calculating the values for  $E_R$  and BP. The algorithms are schematically displayed in the bottom of fig. 11. The hatched areas

indicate the sums over the samples. The control logics (not shown in fig. 11) organizes the coincidence condition with respect to the PSAC, a pile-up inspection, and the connection with the first-level trigger. The digital-processing system (two CAMAC modules per FOBOS module) is very simple to operate, faster than a conventional one by a factor of  $\approx 10$ , and about two times cheaper. An energy resolution of the BIC of 89 keV has been achieved for  $^{238}\text{Pu}$   $\alpha$ -particles.

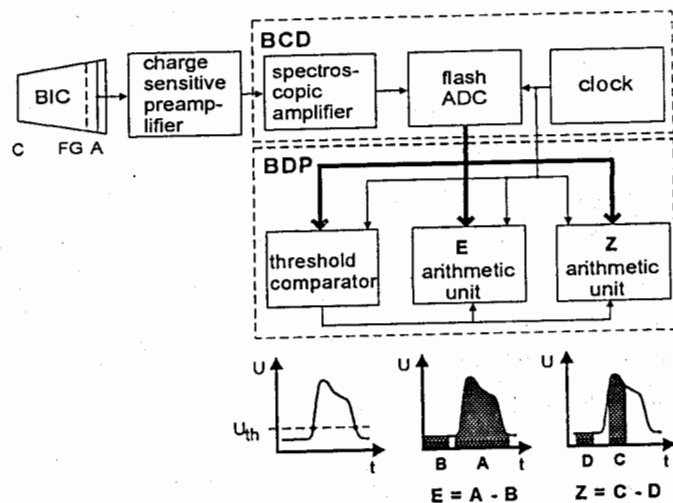
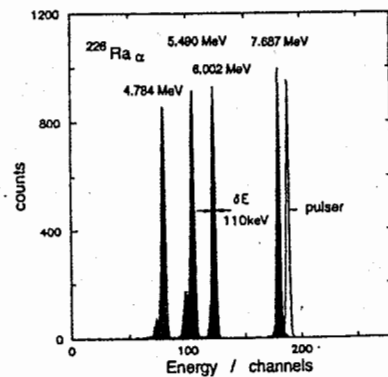


Fig. 11 Principle of the digital-processing method of the BIC signal. (C - cathode, FG A - Frisch grid and anode, BCD - Bragg-curve digitizer unit, BDP - Bragg digital-processor unit) The hatched areas A, B, C, D indicate the sums over the samples.



An energy spectrum measured with a  $^{226}\text{Ra}$   $\alpha$ -source is shown in fig. 12.

Fig. 12 Energy spectrum of a  $^{226}\text{Ra}$   $\alpha$ -source measured by a BIC. The energy resolution at 6 MeV amounts to 1.8 %.

A BP versus  $E_R$  scatterplot measured for the reaction  $^{14}\text{N}$  (34 A MeV) +  $^{197}\text{Au}$  [17] is shown in fig. 13. The charge resolution obtained around Al is  $Z / \Delta Z = 65$ . Elements are resolved from He up to about Fe.

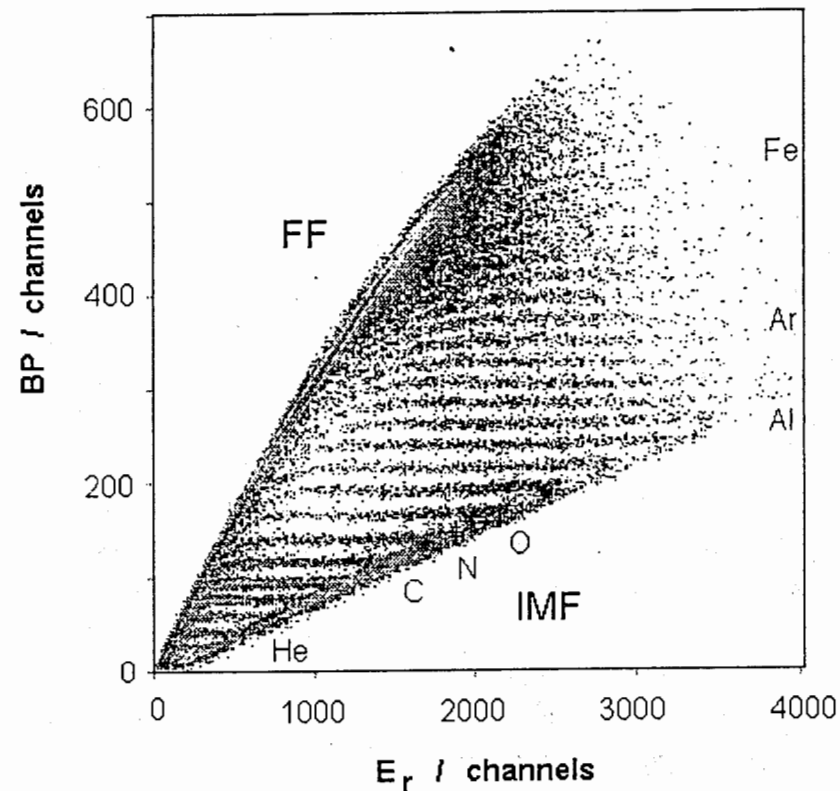


Fig. 13 Bragg peak-height (BP) versus residual energy ( $E_R$ ) scatterplot of inclusive fragments measured by a BIC for the reaction  $^{14}\text{N}$  (34 A MeV) +  $^{197}\text{Au}$ . Particle branches of several resolved elements are indicated. (FF - fission fragments; IMF - intermediate mass fragments)

## 2.4 Evacuation and gas - supply system

The central vacuum chamber is evacuated by three turbomolecular and four cryogenic pumps achieving an effective pumping speed of  $5000 \text{ l s}^{-1}$ . The critical leakage is caused by the pressure-dependent diffusion rate of the chamber gas through the window foils of the BIC. To avoid additional leakage caused by mechanical defects, the supporting Ni-meshes had to be tooled very carefully, and all the foils were checked for leakage at a separate test-stand before they were mounted on the BIC. At a total foil leakage rate of  $\approx 0.2 \text{ mbar l s}^{-1}$ , which is about twice the theoretically expected diffusion rate at typical BIC pressures, an ultimate vacuum of  $\approx 10^{-4} \text{ mbar}$  can be reached inside the central vacuum chamber.

The gas-filled detectors of FOBOS are operated in a flow-through regime to guarantee stable long-time working conditions. To prevent damage of the thin window foils, all manipulations, i.e. the evacuation from atmosphere, gas-loading, gas-flow and gas-pressure stabilization, gas-evacuation, air-inlet etc., have to be carried out in a strict order and with sufficiently long time constants. At every time, a full knowledge of the status of the whole apparatus is necessary. Therefore, a computer-controlled evacuation and gas-supply system has been developed [18, 19].

The gas-detector modules are divided into 10 independently operated groups of three modules each. The inputs and outputs of the PSAC and BIC are connected via individual valves and flexible pipes to collector rings, situated at the front- and rear side of FOBOS (fig. 2), and further to the mass-flow regulators of the gas-inlet and the pressure stabilizers and evacuation system, respectively.

Special sensors and mini-valves are mounted directly to the PSAC frames to limit the pressure gradients at the PSAC to a value of  $\approx 1500 \text{ Pa}$ . In the case of accidental pressure mismatching the mini-valves immediately connect the PSAC volumes with the central volume. The total leakage rate through the PSAC window foils is about one order of magnitude lower than that through the BIC window foils.

The P-10 gas for the BIC is mixed on-line by controlling the respective mass-flows of the components. A gas analyzer permanently checks the gas composition that came out as necessary test for fixing the electron drift-time and, therefore, the energy resolution of the BIC during long-time experiments. Certain series of tests have been performed to optimize the gas flow-through regime. For example, the influence of the gas quality on the signal magnitude of a BIC [20] is shown in fig. 14. The gas exchange rate of the BIC can be adjusted at the inlet

collectors. A full gas exchange takes about 6 hours. All pressures are stabilized to an accuracy of 1 %.

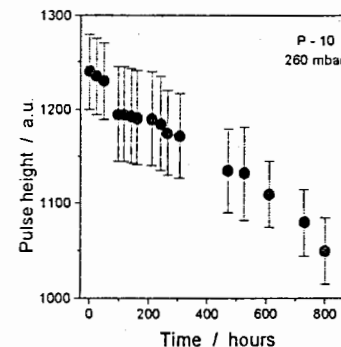


Fig. 14 Influence of the changing gas quality on the signal pulse-height of a BIC operated in a stationary regime with P-10 at a pressure of 260 mbar.

The computer control of the evacuation and gas-supply system of FOBOS is based on a Siemens SX Automation System including graphical visualization of the status on an X-terminal (fig. 15).

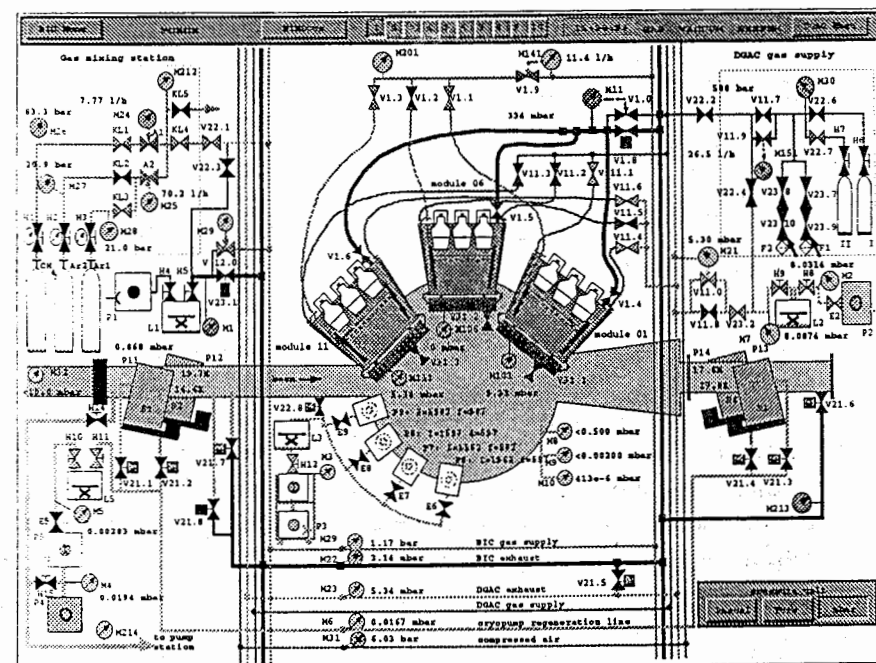


Fig. 15 Graphical visualization of the status of the evacuation and gas-supply system on an X-terminal. The remote control of some evacuation devices is possible.

The actual pressures at 63 measuring points and the gas flows through 11 regulators are recorded in time by a SUN Sparcstation SLC and visualized for check. A full protocol of the operation of the system is created (fig. 16).

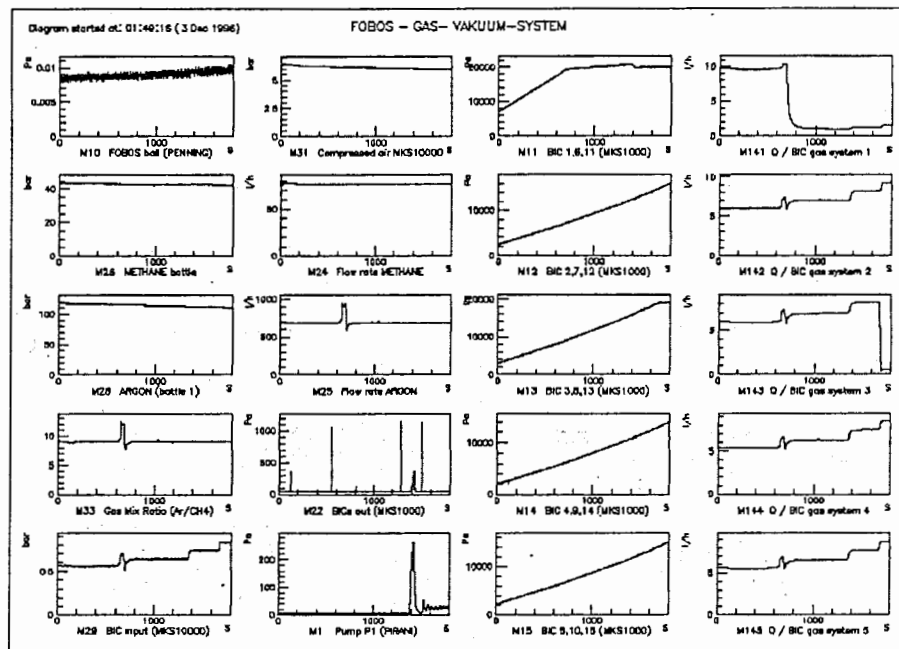
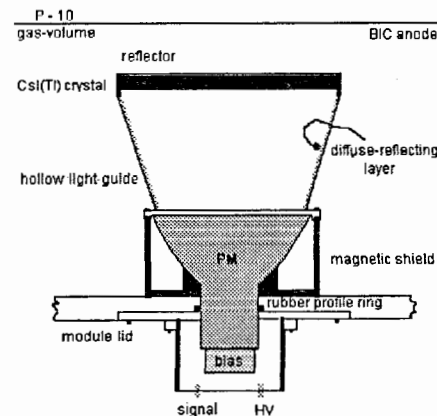


Fig. 16 Snapshot of the on-line protocol of the operation of the evacuation and gas-supply system generated on the SUN SparcSLC terminal.

As an example, the process of the controlled gas inlet into the BIC (M11 - 15, third column) is shown. The immediate reactions of the vacuum in the central chamber (M10), of the P-10 gas pressure at the BIC input (M28), of the methane and argon flow rates (M24, M25), the stability of the on-line gas mixing ratio (M33), and the pumping speeds at the BIC outputs (M142 - 145) are followed in time to avoid any damage in the gas-detectors.

## 2.5 Scintillator shell

A shell of CsI(Tl)-detectors [7] is arranged behind the BIC to register low ionizing LCP and energetic IMF which penetrate the gas-filled detectors. It consists of 210 hexagonal-shaped crystals of thickness 15 mm and 10 mm at angles of  $\vartheta \approx 19^\circ \div 52^\circ$  and  $\vartheta \approx 53^\circ \div 162^\circ$ , respectively. These thicknesses allow to stop protons and  $\alpha$ -particles with energies up to 64 AMeV and 50 AMeV, respectively. The angular resolution is limited by the dimensions of the crystals to  $10^\circ \div 12^\circ$ .



The scintillators are coupled by hollow diffuse-reflecting light-guides to large-area spectroscopic photomultipliers of the types FEU 167 ( $\varnothing$  120 mm) and FEU 173 ( $\varnothing$  170 mm) (fig. 17). A 2  $\mu$ m thick aluminized Mylar reflector in front of the crystals enhances the light output.

Fig. 17 Sketch of the general lay-out of a CsI(Tl) scintillation detector (PM-photomultiplier).

The detector was optimized to have a considerably small position dependence of the light collection ( $\approx 5\%$ ) and a typical energy resolution of  $\approx 8\%$  for  $\alpha$ -particles of 5 MeV energy [7]. The photomultipliers are surrounded by cylindrical magnetic shields.

The LCP-identification is carried out by application of the pulse-shape analysis method [22]. Governed by the intrinsic features of Tl-activated CsI the pulse-shape of the scintillation light depends on the ionization density of the incoming particle. The pulse-shape is characterized by several components of different decay times. The decay time of the fast component ( $\tau_{FAST}$ ) and the ratio of magnitudes of the main slow to the fast component ( $h_{SLOW} / h_{FAST}$ ) are smoothly decreasing functions of the stopping power ( $dE / dx$ ) [23]. Integrating the current signals of the photomultipliers within two well-adjusted timing gates (FAST :  $\Delta t_1 = 0 \div 400$  ns; SLOW :  $\Delta t_2 = 1600 \div 3600$  ns) LCP with  $Z \leq 3$  are well separated for their atomic and mass numbers. A scatterplot illustrating the LCP-identification is given in fig. 18.

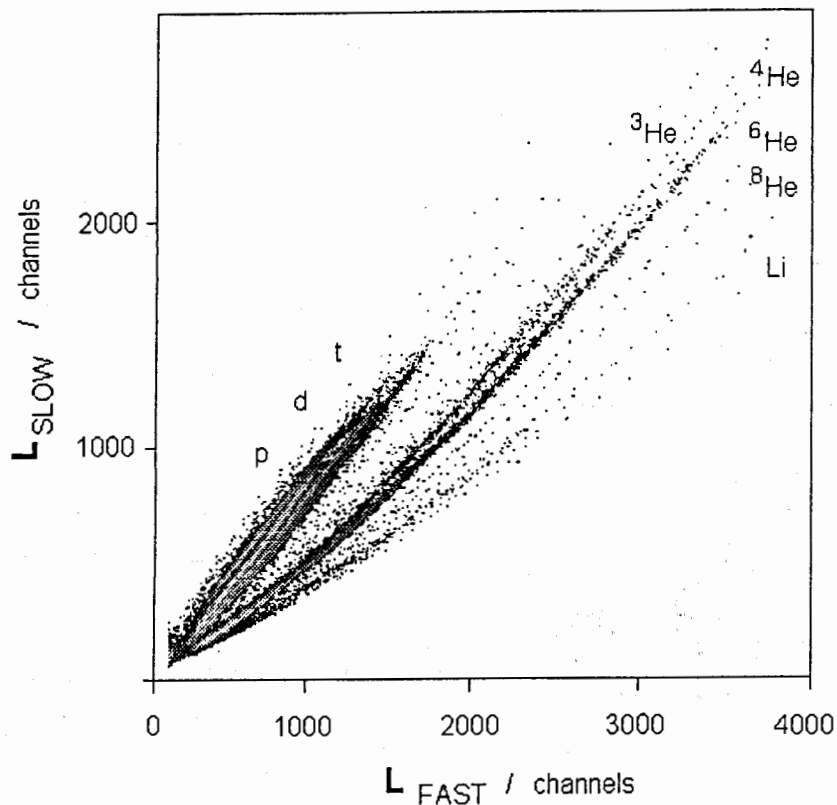


Fig. 18 Scatterplot of the LCP-identification matrix ( $L_{SLOW}$  versus  $L_{FAST}$ ) measured by a CsI(Tl) scintillation detector applying the pulse-shape analysis method. The particle branches of protons, deuterons, tritons, He-isotopes and Li-isotopes are indicated.

Correlated events in a PSAC and a scintillation counter image the geometry of the CsI(Tl)-crystal (fig. 19). The particle identification of such events (e.g. energetic IMF penetrating the BIC) can also be performed by application of the  $\Delta E$ -E-method (fig. 20) using the energy loss in the BIC ( $\Delta E_{BIC}$ ) and the light output ( $E_S$ ) of the scintillator. By this means the dynamic range of the FOBOS detector is enlarged considerably with respect to IMF spectrometry.

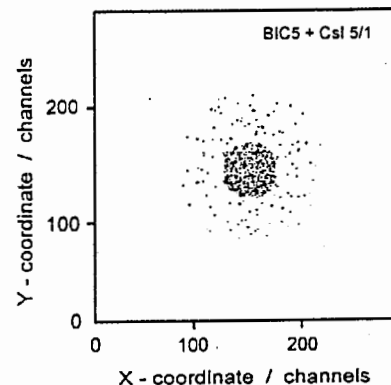


Fig. 19 Coordinates scatterplot of correlated events recorded by a PSAC and a CsI(Tl)-detector positioned behind it. The geometry of the CsI(Tl)-crystal is imaged.

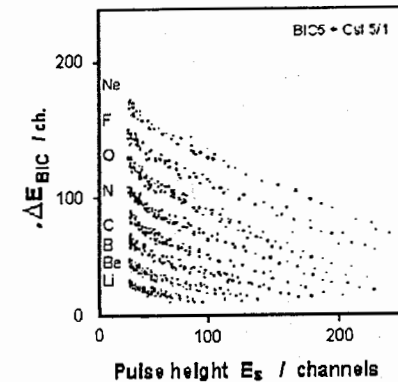


Fig. 20 Charged-particle identification matrix measured by application of the  $\Delta E$ -E-method. ( $\Delta E_{BIC}$  - energy loss in the BIC;  $E_S$  - residual pulse - height of the fast part ( $L_{FAST}$ ) of the CsI(Tl)-detector signal )

## 2.6 Forward array

For geometrical reasons the minimum acceptance angle of the FOBOS spectrometer is  $\vartheta \approx 21^\circ$ . Forward-directed fast reaction products are not registered by the gas detectors. Therefore, part of the former ARGUS detector array [24] has been modified for use as a forward array at FOBOS. It can be installed inside the central vacuum chamber through the forward (exit) cone (fig. 2). The detector geometry of the forward array is given in tab. 2.

The forward array consists of six concentric rings of altogether 92 phoswich detectors, each being a combination of a 0.5 mm thick fast scintillator (Pilot-U) and 20 mm thick slow BGO scintillator. This allows to stop protons ( $\alpha$ -particles) with energies up to  $\approx 100$  AMeV. The element identification is possible up to  $Z \approx 15$  with a threshold for LCP of  $\approx 5$  AMeV.

A simple pulse-processing concept [25] has been modified for its application to phoswich detectors. The principle is to separate the fast component ( $L_{FAST}$ ) of the phoswich light pulse ( $L_{TOTAL}$ ) by certain analog differentiation of the current signal of the photomultiplier. Then only two integration gates ( $\Delta t_{FAST} = 100$  ns and  $\Delta t_{TOTAL} = 400$  ns) common for all phoswich detectors are necessary.

A particle-identification matrix ( $L_{FAST}$  versus  $L_{TOTAL}$ ) of a phoswich detector measured for the reaction  $^{40}\text{Ar}$  (36 AMeV) +  $^{248}\text{Cm}$  is given in fig. 21. Fast projectile-like fragments (PF) can be observed at all possible  $Z$ , and also particle branches of H- and He-nuclei and light IMF. Since the element resolution of a phoswich detector strongly depends on the exact setting of the integration gate for the fast component, a slightly worse resolution compared with the case of using individual integration gates for all the detectors [24] is expected. Nevertheless, this read-out system is very compact and less expensive.

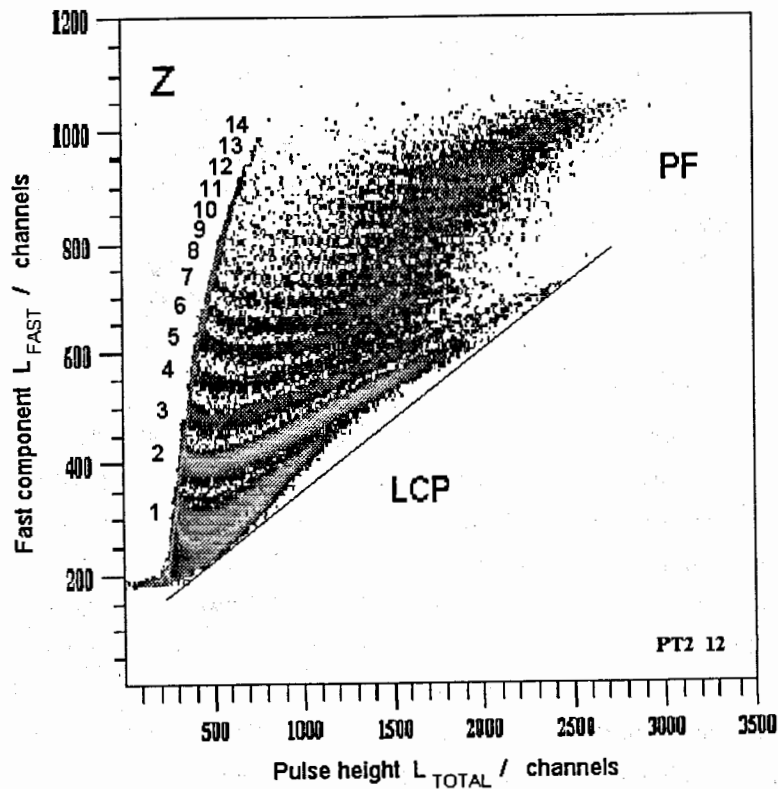


Fig. 21 Charged - particle identification matrix ( $L_{FAST}$  versus  $L_{TOTAL}$ ) measured by a phoswich detector of the forward array at  $\theta = 8^\circ$  for the reaction  $^{40}\text{Ar}$  (36 AMeV) +  $^{248}\text{Cm}$  (PF - projectile-like fragments,  $Z$  - atomic number of charged particles identified).

### 3. DATA ACQUISITION SYSTEM

#### 3.1 First - level trigger

The first-level trigger of FOBOS [21] is usually generated by the gas detector part, and the scintillators are read-out in the slave mode. In special cases a trigger can also be generated by the scintillator shell and/or the forward array. The entire TTL/ECL-based hardware of the trigger logics fills one CAMAC crate. It delivers either the LAM demand for data storage or a general RESET after a certain event inspection leading to a rejection of the event.

Provided the digital processor (BDP) is not busy, a timing signal of the corresponding PSAC passes a special blocking and pile-up inspection unit (LBIN) connected with the control logics of the BDP, opens an event gate of duration  $\Delta t = 200$  ns, sets a bit in the coincidence pattern register and starts a TDC which will be stopped by the next arriving RF-signal from the cyclotron. The event pattern is analyzed by a majority coincidence unit connected with the central event selector which induces a LAM demand if a preset multiplicity condition was fulfilled and there was no signal pile-up. Optionally, the following conditions may be used either to reject the event or to label the affected parameters :

- (i) There is another PSAC signal in the time intervals  $12 \mu\text{s}$  before and  $6 \mu\text{s}$  after the event, respectively.
- (ii) There was another BDB threshold-comparator response in the time interval  $10 \mu\text{s}$  before the event.
- (iii) The trailing edge at the threshold-comparator of the BDP is out of a certain time interval related to the maximum electron drift-time of the BIC.

After a LAM demand has been recognized, the VME processor first reads the coincidence pattern register and then the conversion results of the TDC's (TOF) and BDP's ( $B_P$ ,  $E_R$ ) which had fired. Subsequently, the QDC's of the scintillator shell and the forward array are serviced. Consequently, the blocking signals (BLK) of the LBIN's are removed, and the system is ready for handling the next event.

The counting rates of events of different fragment multiplicity naturally differ by orders of magnitude. A special unit (major divider) which allows to modify the accepted rates concerning the event multiplicity has been developed to optimize the data storage.

A principal scheme of the front-end electronics of a gas-detector module and part of the first-level trigger is shown in fig. 22.

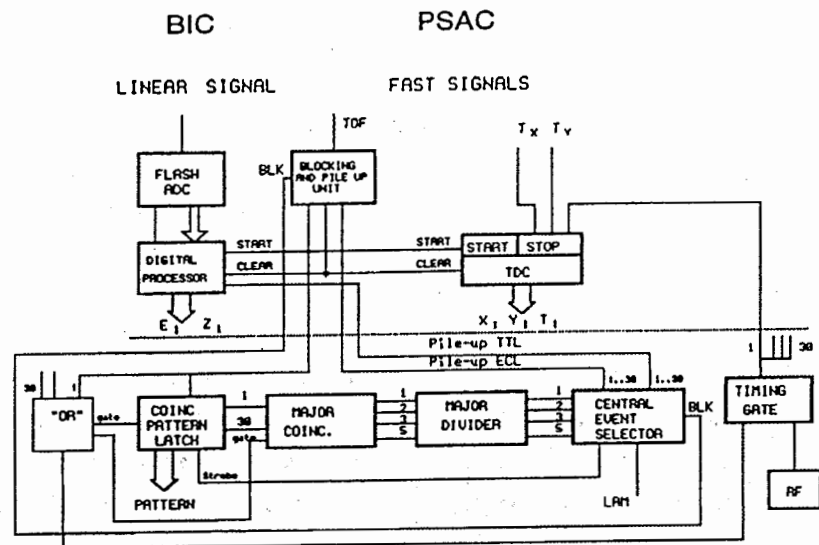


Fig. 22 Front - end electronics of a gas - detector module and part of the first - level trigger. (LAM - "look-at-me" CAMAC signal; BLK - blocking signal; RF - radiofrequency signal from the cyclotron)

### 3.2 Read - out electronics

Ten CAMAC crates housing the digitizing electronics of the gas-detector part and the control logics, and one FASTBUS mini-crate used for the photomultiplier read-out of the scintillator shell and the forward array, are connected with a main VME crate by means of the parallel VSB Differential Bus Extension (VDB bus). The VDB bus is well suited for multi-crate systems where different bus standards have to be controlled. A single-board computer EUROCOM-6 with a 68030 CPU builds the event data blocks [26].

The CAMAC-to-VSB interface is a single-width CAMAC crate controller STR 610 / CBV [27] driven from the VME Subsystem Bus (VSB) via the VSB Differential Cable. The specification of the CBV is similar to the CAMAC crate controller of type A1. It maps a portion of the VSB address space to the CAMAC - "C,N,A,F" and generates single CAMAC cycles from each proper VSB cycle.

The FASTBUS mini-crate contains a 68030-processor board (CERN Host Interface; CHI), an I/O-Port, a LAN Ethernet module [27] and six 96-channel FASTBUS QDC's (C.A.E.N. F683C [28] and LeCroy [29]). The VSB I/O-Port provides an efficient interface between the CHI and the VME workstation where the CHI is operating in the VDB slave-mode. The CHI data memory is directly mapped into the local VSB address space, and the EUROCOM-6 processor module is treated in the same manner as any local memory.

The VME workstation sends the data blocks via Ethernet (LAN) and a fiberoptical link to a SUN Sparcstation-10 which writes them "event by event" to the mass storage memory. The architecture of the data acquisition system is schematically shown in fig. 23. The maximum data rate with respect to the gas-detector part of FOBOS is about 200 kbyte s<sup>-1</sup>. Due to the conversion time of the FASTBUS QDC's (1 ms) residual rates of 50 ÷ 100 kbyte s<sup>-1</sup> are typical for the whole spectrometer. Therefore, the maximum permitted counting rate of FOBOS becomes ≈ 500 ÷ 1000 events s<sup>-1</sup>. It is mostly restricted by other experimental considerations like, e.g., the rate of random coincidences etc.

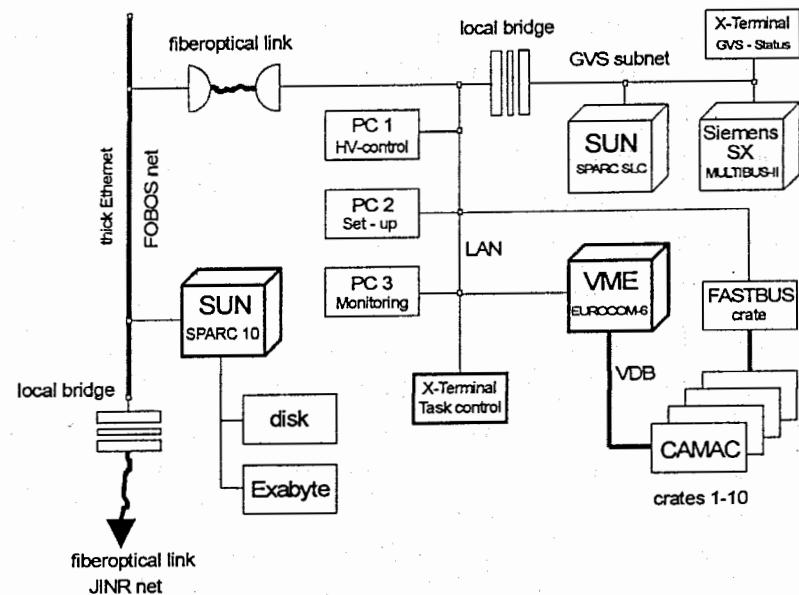


Fig. 23 Architecture of the data acquisition and the gas-vacuum system (GVS) network. (LAN - local net; VDB - VSB differential bus)

The EUROCOM-6 and the CHI are operating under the Microware real-time operating system OS-9 (professional). All time-critical tasks are moved to the module processors. The data acquisition control program (TINH) runs on the SUN Sparcstation -10.

Quasi-on-line monitoring of the recorded data is performed using several AT 486 personal computers (PC) and the ATHENE data analysis software [30] which via LAN organizes a direct access to the data just written to the disk memory of the SUN Sparcstation-10.

### 3.3 Experimental data structure

The list-mode data structure is adopted from the VMS-based data acquisition system HOOPSY [31] in order to use the available OLYMP data analysis package [32]. It is module-oriented by an event-pattern register containing information about fired PSAC, CsI(Tl)-detectors and groups of phoswich detectors. Up to 10 parameters can be defined to be read out in correlation with one pattern bit, and altogether 2000 parameters can be handled by the program TINH. In average, a valid event is characterized by 20 ÷ 30 parameters which are stored within  $\approx 2.5$  ms.

The data file structure is characterized by sequential event storage into closed blocks of fixed length (512 byte). A header containing information about the data file structure (defined parameters) is assigned to the ATHENE program for quasi-on-line or off-line data analysis.

### 3.4 Data analysis software

The ATHENE code [30] was especially designed for a distributed analysis of the data obtained at the FOBOS spectrometer using IBM PC's of type AT 386/486. A new more powerful version (ATHENE94) [33] written in the object-oriented language C++ [34, 35] has been developed for real-time data processing on computers with UNIX-like operational systems and an X-WINDOWS environment [36].

The program allows to read data written in the formats of the programs CAMDA [37], HOOPSY [31] and OLYMP [32]. Special transformation algorithms to read data written in other formats are available.

Via the menu, the user has the possibility to accumulate and to visualize up to 20 ordinary histograms and up to 50 color scatterplots, he can produce new data files reduced in the event dimension and/or selected by sorting conditions (gates) in the formats of CAMDA or

OLYMP, he can execute a number of analysis operations acting to these histograms such as simultaneous displaying of several histograms, linear/logarithmic scaling, setting gates within the histograms or scatterplots, calculating spectrum parameters and statistics, etc. He can interactively drive the process of data accumulation by setting both the parameters and relevant selection criteria for every histogram, scatterplot or output data file. All the configuration conditions concerning parameters, histograms, plots, gates, selection criteria, etc. as well as the content of any histogram or plot can be saved to a disk file and retrieved.

## 4. CALIBRATION PROCEDURES

### 4.1 Parameter calibration for the gas - filled detector modules

The application of gas-filled detectors for the measurement of charged particles implies one important advantage, namely the linear and charge-independent correlation between the stored raw data and the corresponding physical values. Hence, the transformation of the measured data — the PSAC-coordinates (X,Y), the fragment TOF and energy  $E_R$  — into physical units requires the determination of only two calibration constants for each of the parameters.

However, in any case it is necessary to catch some events within the collected spectra, which result from fragments with known quantities. A well established practice to generate such events is to carry out special measurements with calibration sources ( e.g.  $\alpha$ -particle emitters or spontaneously fissioning nuclides) or the impinging of elastically scattered beams. Unfortunately, this method involves some general difficulties. The first of them is caused by the energy loss of any fragment within the target layer. Furthermore, the general requirement of identical conditions for the calibration and the data taking measurements fails.

An alternative method applied in the present work is described below. The procedures used deliver an intrinsic calibration based on the original raw data only. For convenience the measured parameters (in channel units of the ADC devices) are further on denoted in capital letters, the calibrated physical values (in units of cm, ns, MeV etc.) in small letters.

#### 4.1.1 Coordinates calibration of the position-sensitive avalanche counters

The absolute coordinates calibration of the PSAC is performed by using coordinates scatterplots of events measured in coincidence with the BIC positioned behind them. The supporting structure of the window foil of the BIC generates a shadowed zone of decreased



rate (fig. 7). A geometrical model of the supporting structure is adjusted to the center and to the dimensions of this image to achieve a complete agreement with the shadowed zone. This procedure gives the intrinsic scales which are used to define the module-oriented coordinates (x,y) of the registered event. The polar and azimuthal angles ( $\theta, \phi$ ) of the particle with respect to the target position can be calculated in a straight-forward manner referring to tab. 1. The uncertainties ( $\Delta x, \Delta y$ ) lead to errors of  $\Delta\theta = \Delta\phi \approx 0.2^\circ$ .

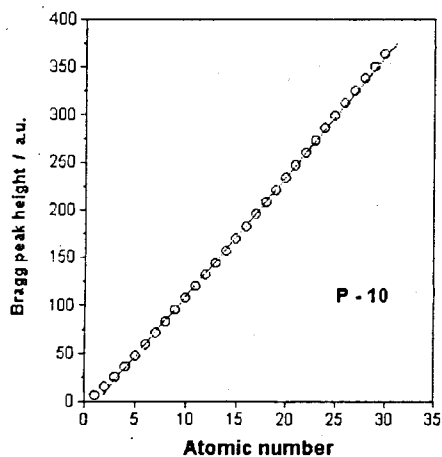
#### 4.1.2 Energy calibration of the Bragg chambers

The calibration procedure for the residual energy ( $E_R$ ) of the fragments in the BIC makes use of the additional information concerning the fragment charge (Z), which is in particular available for IMF from the Bragg-peak spectroscopy. This method of charge determination requires that the maximum of the energy-loss distribution (Bragg-curve) of the fragment considered is located inside the sensitive volume of the BIC, accurately said, between the cathode and the Frisch grid. In this case the measured Bragg peak-height (BP) is independent on the entrance energy of the fragment.

An analytic expression of the dependence of BP on Z of particles stopped in a P-10 gas-mixture has been derived in ref. [38],

$$BP(Z) = C \cdot \exp(-18.95 \cdot Z^{-0.0721}) \quad (1)$$

where C denotes a scaling factor which has to be determined experimentally. In a wide range



the function BP(Z) can be rather well approximated by a linear expression (fig. 24). This leads to the nearly equidistant particle branches observed in fig. 13.

Fig. 24 Dependence of the Bragg peak-height (BP) on the atomic number (Z) of charged fragments stopped in a P-10 gas-mixture. The calculated values (eq. 1) are indicated by open circles. The line results from a linear regression analysis. It is defined by the expression

$$BP(Z)_{lin} = C \cdot (12.511 \cdot Z - 15.518).$$

In practice the measurement of the Bragg-peak requires a considerably large entrance energy, especially for heavier fragments. The lower energy threshold depends on the operation parameters of the BIC and the pulse-processing method, i.e. the electron drift velocity, the gas pressure, the integration time constant of the current pulse, and the total time interval of energy-loss integration. At typical operation conditions, the minimum necessary energy loss of an IMF for Z-identification amounts to  $e_R^{\min} \approx 0.6$  AMeV.

If the fragments are stopped in the gas-volume of the BIC, the measured value  $E_R$  reflects the residual fragment energy at the entrance into the chamber gas (if the nuclear stopping is neglected or corrected for).

The situation changes for such kinetic energies which allow the fragments to pass through the entire chamber depth. In this case the energy loss within the gas-volume decreases with increasing entrance energy. This results in an upper limit for direct residual-energy measurement ( $e_R^{\max}$ ) and charge identification. It strongly depends on the composition and the pressure of the chamber gas, on the path length within the BIC, and on (A,Z) of the fragments. The upper energy thresholds  $e_R^{\max}$  of the BIC have been calculated for particles of  $Z = 2 \div 10$  ( $A = 2 \cdot Z \pm 1$ ) at P-10 pressures of 19, 32 and 45 kPa (fig. 25) by use of the range-energy code STOPOW [39]. The dependence of the specific energy loss on A was approximated by the range parametrization  $R/A = r(E,Z)$ .

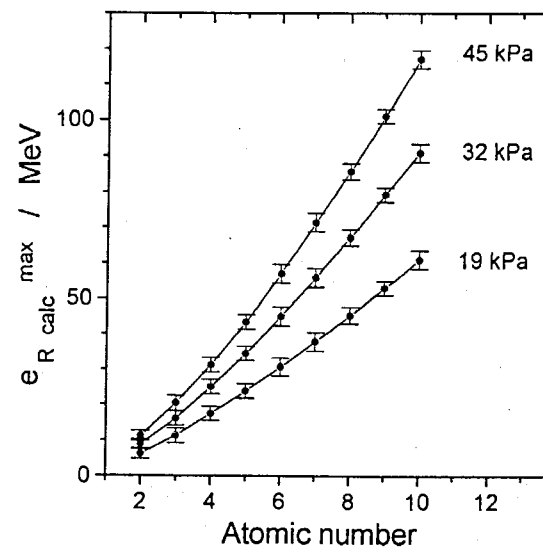


Fig. 25 Maximum energy losses in the gas-volume of the BIC ( $e_{R, calc}^{\max}$ ) calculated for selected particles at pressures of the P-10 gas-mixture of 19, 32 and 45 kPa.

Under the condition of sufficient statistics, the energy points  $E_R^{\min}$  and  $E_R^{\max}$  can easily be fixed for resolved Z-branches in the raw-data matrix BP versus  $E_R$  (fig. 13).

However, in particular at small  $Z$ , particle branches of different isotopes can overlap (fig. 26). This complicates the unambiguous fixing of  $E_R^{\max}$ .

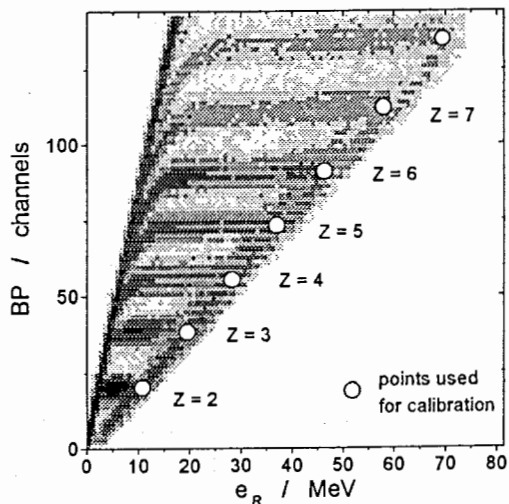


Fig. 26 Part of a BP versus  $E_R$  scatterplot of a BIC (cf. fig. 13). The events have been stored with respect to the calibrated energy scale ( $e_R$ ). The points used for the calibration procedure are marked.

In addition to these calibration points, the BDB [16] guarantees that the value  $E_R = 0$  corresponds with the ADC channel number "zero". The

remaining slope constant for the energy-calibration curve  $e_R(E_R)$  is deduced by a linear regression analysis (fig. 27).

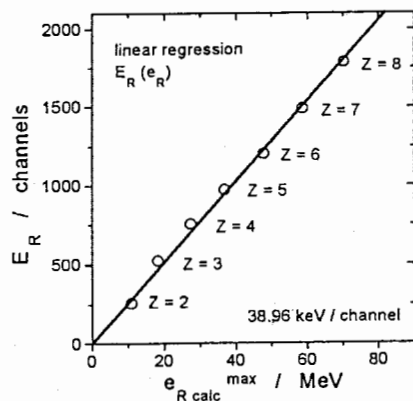


Fig. 27 Energy-scale calibration of the BIC by the comparison of the calculated maximum energy losses ( $e_{R \text{ calc}}^{\max}$ ) with the corresponding values  $E_R$  measured for particles of  $Z = 2 \div 8$ . A linear regression analysis (line) delivers the slope constant of the calibration curve.

In order to perform a relative scaling between the BP-spectra of different BIC's, the identified  $Z$ -branches are used for the determination of an "experimental" function  $BP(Z)^{\text{exp}}$ . (Note that this intrinsic calibration does not relate to eq. 1!). A BP-spectrum of events

selected by gates over the energy intervals  $E_R^{\min} < E_R < E_R^{\max}$  for each  $Z$ , respectively, is shown in fig. 28.

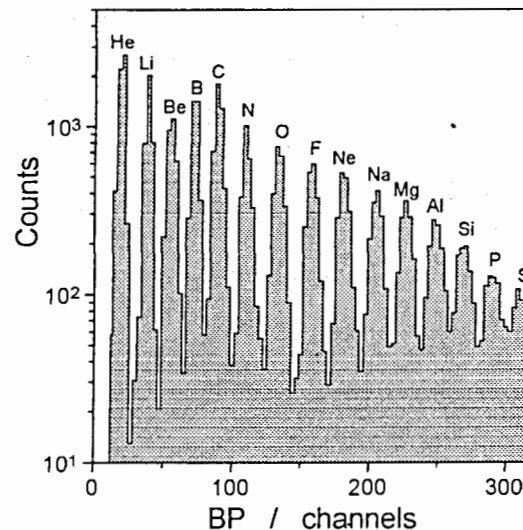


Fig. 28 BP - spectrum of selected fragments at kinetic energies corresponding to the maximum specific energy losses (Bragg-peaks).

The mean values  $\langle BP \rangle$  of the peaks are compared with the corresponding  $Z$  in fig. 29. A linear regression analysis delivered the function  $BP(Z)^{\text{exp}}$  which can be used for scaling purposes.

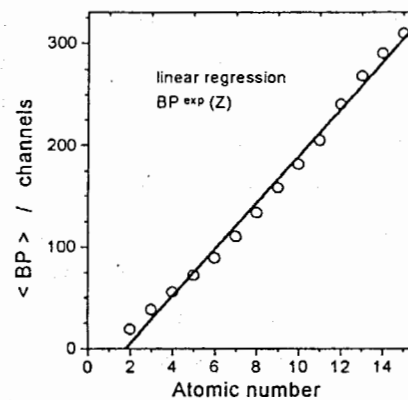


Fig. 29 Correlation between the mean measured BP-values of the fragments and the corresponding atomic numbers ( $Z$ ) for the same events as in the BP-spectrum shown in fig. 28. A linear regression analysis delivers the "experimental" scaling function  $BP^{\text{exp}}(Z)$ .

### 4.1.3 Time calibration of the position-sensitive avalanche counters

The absolute TOF calibration necessary for the determination of the fragment velocities is based on data selected for identified Z, calibrated  $e_R$  and  $(\vartheta, \phi)$ . The mass number A for a given Z has been estimated with respect to the line of  $\beta$ -stability. The geometrical set-up together with the calibrated coordinates  $(x, y)$  define the individual TOF path-length  $d(x, y)$  of the fragments from the target to the PSAC considered. Taking into account all the parameters known up to now, the energy losses  $\Delta e_i(Z, A, e_R, n_i)$  in the k detector foils of areal density  $n_i$  are successively calculated, starting from the entrance window of the BIC and following "backward" to the entrance foil of the PSAC. For simplicity it is assumed in the following that the fragment velocity is *constant* on the TOF path-length (d), but this procedure is also applicable in the general case, i.e. accounting for some energy loss *on* d (e.g. in the PSAC window foil). The *tof* of the fragments can thereby be determined by eq. 2,

$$\text{tof}^2 = A \cdot d(x, y)^2 / 2 \left[ e_R + \sum_{i=1, k} \Delta e_i(Z, A, e_R, n_i(x, y)) \right] \quad (2)$$

and compared with the TOF "event by event". The correlation between *tof* and TOF (eq. 3) is shown in fig. 30.

$$\text{tof} = (\text{TOF} - \text{TOF}_0) \cdot \delta \text{tof} / \delta \text{TOF} \quad (3)$$

The slope constant  $\delta \text{tof} / \delta \text{TOF}$  is determined with an accuracy of  $< 0.5\%$  by use of a time-calibration pulse-generator. Hence, the absolute time-scale (eq. 3) only depends on the constant  $\text{TOF}_0$  which can be determined from the curve *tof*(TOF) obtained by a linear regression analysis (fig. 30).

Evidently, there is a strong dependence of the resulting absolute time scale on the energy calibration as well as on the calculation of the energy losses  $\Delta e_i$ . It should be noted, however, that the energy losses within the target layer *do not influence* the calibration at all.

With the aim to check the consistency of this calibration procedure, a test measurement has been carried out using a  $^{252}\text{Cf}$ (sf) source. An additional transmission avalanche counter was mounted near the target position to generate the START-signal for the TOF-measurement. (Else the timing reference signal is given by the RF of the cyclotron.) In this way the time calibration could be performed by means of a TOF-TOF-analysis for the paired fission

fragments recorded by two opposite detector modules. The absolute time-scale deduced from the TOF-TOF-analysis agrees with the time calibration described above within  $0.5 \pm 1$  ns.

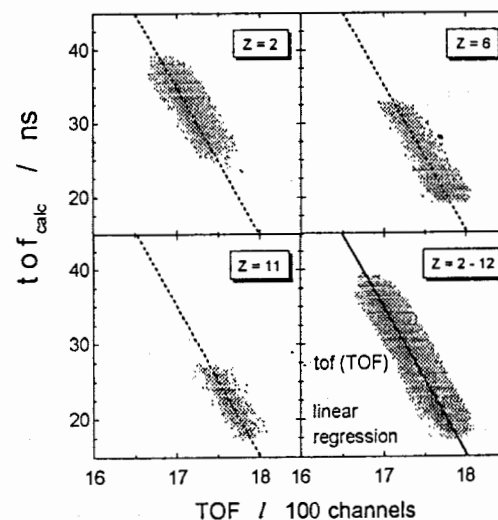


Fig. 30 Absolute calibration of the TOF-scale. The measured values (TOF) are compared with those calculated by eq. 2 (*tof<sub>calc</sub>*) for selected events generated by particles with known parameters. A linear regression analysis delivers the curve *tof*(TOF) for the determination of the constant  $\text{TOF}_0$  of eq. 3.

## 4.2 Calibration of the scintillation detectors

Since the total integrals of the light pulses of the CsI(Tl)-scintillators were not recorded, the energy calibration is performed by comparison of simulated and measured particle-identification branches (fig. 18) [40]. A model of a two-component pulse-shape  $L(t)$  for LCP (eq. 4) has been normalized to the non-linear and particle-dependent response of CsI(Tl) (eq. 5) [41],

$$L(t) = (h_{\text{FAST}} / \tau_{\text{FAST}}) \cdot \exp(-t / \tau_{\text{FAST}}) + (h_{\text{SLOW}} / \tau_{\text{SLOW}}) \cdot \exp(-t / \tau_{\text{SLOW}}) - (h_{\text{FAST}} / \tau_{\text{FAST}} + h_{\text{SLOW}} / \tau_{\text{SLOW}}) \cdot \exp(-t / \tau_{\text{FRONT}}) \quad (4)$$

$$L(E, Z, A) = S \cdot [E - a(Z, A) \cdot \ln(E / a(Z, A) + 1)] \quad (5)$$

where  $\tau_i$  are the rise- and decay time constants of the scintillation light pulse,  $h_i$  denote the magnitudes of the light components, S is the absolute scintillation efficiency, and  $a(Z, A)$  is a particle-dependent quenching constant.

Using appropriate empirical functions for the dependence of  $\tau_{FAST}$  and of the ratio  $h_{SLOW} / h_{FAST}$  on the particle type ( $Z, A$ ) and energy ( $E$ ), and performing the integration of  $L(t)$  within the set time gates ( $\Delta t_1, \Delta t_2$ ) a particle-identification matrix has been simulated (fig. 31a). The punch-through energies of protons, deuterons and tritons were used for adjusting the simulated to the measured particle-identification matrices. Additional normalization points are delivered by the tof of low-energy  $\alpha$ -particles registered by the PSAC and stopped in the scintillators. The simulated particle-identification matrix then defines the absolute energy scales for all LCP simultaneously [40] (fig. 31b).

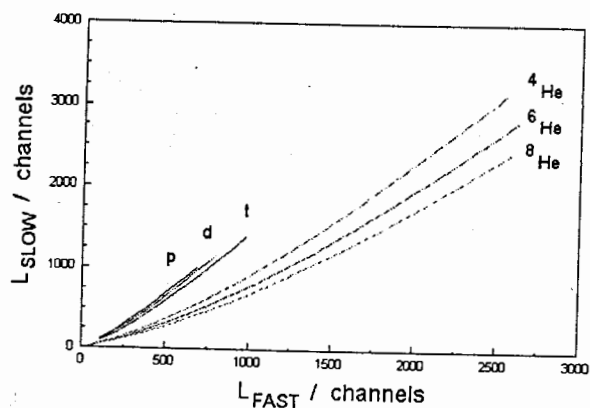
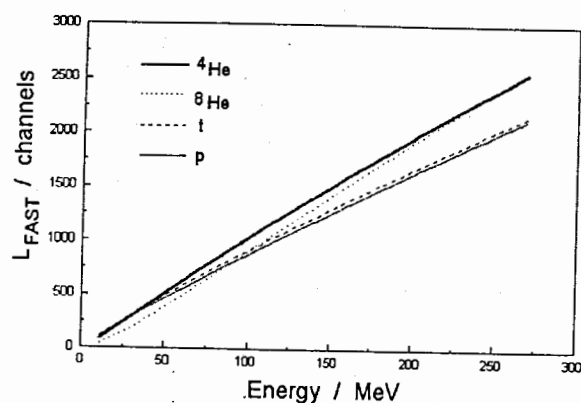


Fig. 31 Simulation of the particle branches of an LCP-identification matrix for CsI(Tl) as it follows from the application of the pulse-shape analysis method (a).



Energy-calibration curves for several LCP (b).

The calibration of the phoswich detectors of the forward array has been described earlier in ref. [24].

## 5. PHYSICAL OBSERVABLES OF CHARGED PARTICLES

In the following we refer to a particle-oriented data set, where every individual fragment ( $Z \geq 2$ ) is characterized by its calibrated parameters ( $\vartheta, \varphi, \text{tof}, e_R$ ). For a large amount of recorded IMF the fragment charge ( $Z$ ) is additionally determined by Bragg-peak spectroscopy. It should be emphasized once more, that the applied calibration procedure *does not suppose any correlation between the fragments* registered in an event.

From the calibrated data further physical observables can be derived, namely the fragment masses ( $m$ ), the primary emission energies ( $e$ ), and, eventually, the velocity- and linear momentum vectors ( $v, p$ ). The main difficulties concerning  $m$  and  $e$  arise from the energy losses of the fragments in the (though very thin) detector foils. Since the energy loss, on the other hand, depends on  $Z$  and  $v$ , the mass determination requires to solve the following system of equations,

$$e_0(\text{tof}, A) = A/2 \cdot (d/\text{tof})^2 \quad (6)$$

$$e_0(e_R, A) = e_R + \sum_{i=1, k} \Delta e_i(e_0, Z(A), n_i) \quad (7)$$

where  $e_0$  is the kinetic energy of the fragment at the START-position of the TOF-measurement. It is obvious that  $e_0$  influences both the parameters  $\text{tof}$  and  $e_R$ . Concerning the fragments not identified by  $Z$ , a suitable  $A(Z)$ -relation has to be introduced into eqs. 6, 7. Since  $\text{tof}$  and  $e_R$  are fixed parameters, the solution of eqs. 6, 7 has to account for the following considerations:

- (i) The effective thickness of the detector foils is a function of the PSAC coordinates ( $x, y$ ). Additional uncertainties can be caused by non-planar surfaces and local nonuniformities.
- (ii) The STOP-signal generated by the PSAC is position-dependent due to electronic signal delays.
- (iii) The  $e_R$ -values have to be corrected for the energy loss by nuclear stopping not contained in  $E_R$ . This so-called ionization defect has been evaluated for P-10 applying the method described in ref. [42]. For fission fragments these corrections amount to  $2 \div 3$  MeV.

For the solution of eqs. 6, 7 an iterative procedure has been developed [43]. However, it turned out that for the extensive data sets typical for a FOBOS experiment this procedure consumes a huge amount of computer-time. The data processing could be accelerated by dividing the task into several steps. —

At first, a set of tables has been generated by means of a simulation code, which calculates a grid of  $(\text{tof}, e_R)$  - spot points for a given  $Z$ . The input data for the calculation of the  $Z(\text{tof}, e_R, F)$ -matrices are defined by the experimental conditions, i.e. the geometry of the set-up, the compositions of the detector materials (window foils, electrodes, gas-filled sections), the thicknesses of the different layers which are assumed to be parallel to each other and planar etc. The factor  $F \geq 1$  considers the position (i.e. angular) dependence of all distances and path lengths through the detector materials. The remaining parameter is the angle  $\varepsilon$  between the emission direction of the fragment  $(\vartheta, \varphi)$  and the common normal of the detector layers. It is determined by eqs. 8, 9,

$$F(x,y) = 1 / \cos \varepsilon(x,y) \quad (8)$$

$$\tan^2 \varepsilon(x,y) = (x^2 + y^2) / L^2 \quad (9)$$

where  $L$  refers to the distance between the target and the plane of the entrance foil of the BIC.

Since the acceptance angle of the large gas-detector module corresponds with an  $\varepsilon^{\max} = 16.8^\circ$ , the effective thickness of any layer penetrated by the fragments can not increase more than 4.5 % with respect to the normal angle of incidence. Therefore, a relatively small number of spot-points within the limited range of  $F$ -values is enough to consider the  $(x,y)$ -dependence with a sufficient accuracy. —

The second step — the determination of  $m$  “event by event” — is based on the calculated tables. At first, the  $F$ -value is deduced, and the  $\text{tof}$  is corrected for its electronic position dependence. By means of a two-dimensional interpolation between relevant spot-points of the tables, an interval  $[Z_1(\text{tof}, e_R, F_1), Z_2(\text{tof}, e_R, F_2)]$  is determined for the fragment charge considering  $F_1 < F < F_2$ . The final result for  $Z$  is obtained from a linear interpolation with respect to  $F$ . Finally, the mass of the fragment can be deduced if the  $A(Z)$ -relation is given.

Since the energy losses  $\Sigma \Delta e_i$  can — in particular for FF — exceed 50 % of the energy  $e_0$ , the most critical moment of the mass determination turned out to be the preparation of sufficiently accurate energy-loss data. They have been calculated by use of the code STOPOW [39] which represents a modified version of the algorithm developed in ref. [44]. A detailed

analysis of the generated range-energy data set, however, indicated that the so-called  $Z_1$ -oscillations, observed for fragments of large  $Z$  at keV-energies [45], are overestimated at energies of  $E/A \leq 1$  MeV/A. This can also be observed in the  $e_R$  versus  $\text{tof}$  plot of fig. 32, which has been calculated for given  $Z$  and  $A(Z)$  at  $F = \text{const}$ . Since different  $Z$ -branches in some areas even overlap, an unambiguous solution of eqs. 6, 7 does not exist.

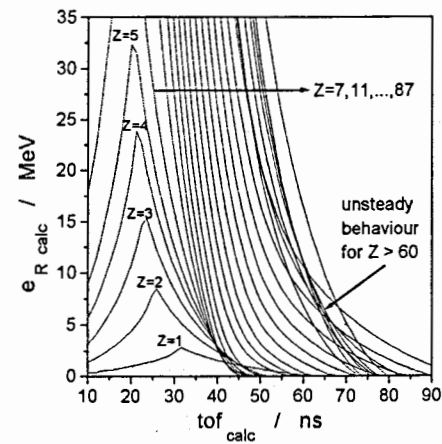


Fig. 32 Calculation of  $e_R$  versus  $\text{tof}$  for a gas-detector module. The lines correspond to different atomic numbers ( $Z$ ) of the particles. The range-energy tables used for the determination of the energy losses were calculated by means of the code STOPOW88.

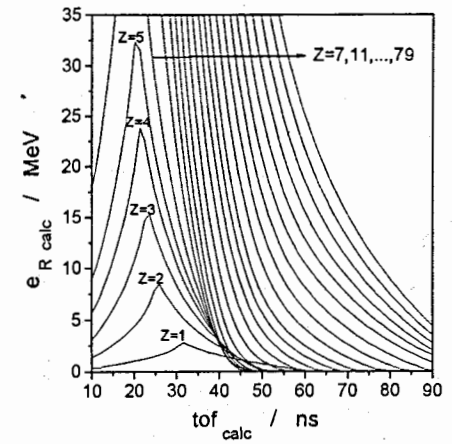


Fig. 33 The same calculation as shown in fig. 32, but by use of the modified range-energy data set (see text) for the calculation of the energy losses. The distance between the lines corresponding to increasing  $Z$  now changes smoothly.

Test measurements with a  $^{252}\text{Cf}(\text{sf})$  source have been carried out to select FF with known mean  $Z$  and  $A$ . Consistency with the calculated  $e_R$  versus  $\text{tof}$  data has been obtained for this  $(Z,A)$  by an appropriate modification of the original range-energy data set. Hence, the data for the remaining  $Z$  were deduced by a suitable interpolation. In this way, an “empirically improved” range-energy data set has been generated, which was used for the calculation of the  $e_R$  versus  $\text{tof}$  plot shown in fig. 33. The relation  $Z(\text{tof}, e_R, A)$  is unambiguous now, and the solution of eqs. 6, 7 does likewise. To check these modified range-energy data, the FF mass distribution determined from the  $^{252}\text{Cf}(\text{sf})$  measurement is compared in fig. 34 with reference data taken from ref. [46]. The peak of the light fragment is well reproduced, the maximum deviation at largest fragment masses is  $\approx 7$  a.m.u. As an analysis showed (see chapter 6.2.1), this approach is even valid up to  $A \approx 190$ . —

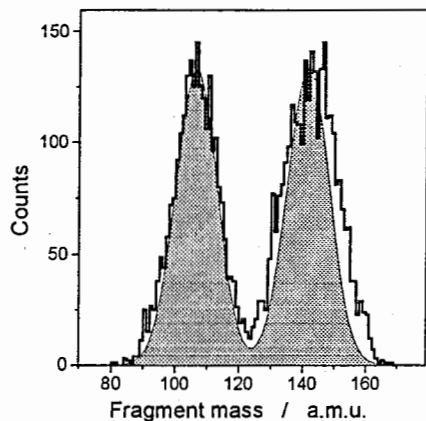


Fig. 34 Mass distribution of fission fragments (histogram) derived from a measurement with a  $^{252}\text{Cf(sf)}$  source. The data of ref. [46] (filled area) are shown for comparison. The spectra are normalized at the peak of the light fragment.

In the third step, the primary emission energy  $e_0$  of the fragment (A,Z) is calculated assuming a mean value for the thickness of the target layer. The areal density of the target is known, but a mean value arises due to the

different emission angles of the fragments with respect to the target normal. In principle, a procedure analog to that applied for the mass determination could be developed with respect to  $e_0$  too. When calculating  $e_0$  (tof,  $e_R$ ,  $x$ ,  $y$ ), however, the additional energy loss of the fragments within the target layer must be taken into account. In the general case, the target layer is positioned under a determined angle, e.g., in relation to the beam axis. This distorts the axial symmetry of the experimental set-up. Therefore, the simple parametrization for  $F(x,y)$  (eqs. 8, 9) is not yet valid, and a correct calculation would require a large number of prepared tables in dependence on the coordinates (x,y). For this reason, the *effective* target thickness and the corresponding energy losses have been calculated "event by event". Considering a value for the ionization defect  $\text{Def}[e_0(A, Z, e_R)]$  as given in ref. [42], the fragment energy  $e_R(E_R)$  at the entrance into the gas-volume of the BIC is used to simulate the history of the particle "backward" to the target. In this manner, both  $e_0$  and tof were calculated as described in section 4.1.3. —

In the further analysis, the calculated tof is used to check the main condition for a correct determination of  $e_R$ , namely, that any calculated value must agree with the measured one if the fragment was stopped within the gas-volume of the BIC. Otherwise — if the fragment passed through the BIC and there lost a sufficiently large amount of energy — the tof calculated for this fragment is significantly *larger* than the measured one. In this case, the  $e_R$  deduced from  $E_R$  is changed to higher values until the calculated tof agrees with the measured one. This last procedure allows to determine the  $e_0$  also for those fragments which penetrated the BIC (mainly light IMF). —

Finally, the linear momentum vectors ( $p_i$ ) of all the fragments (i) emitted in one event can be obtained from the individual ( $\vartheta$ ,  $\varphi$ ,  $v$ , A, Z). The accuracy of  $p$  is mass-dependent. It amounts to  $\sigma_p / p \approx 3\%$  for FF of  $^{252}\text{Cf(sf)}$ .

## 6. EXPERIMENTS AT FOBOS

In this chapter, some performance of the spectrometer FOBOS is discussed. The main aim is more an illustration of the quality of measurements at low fragment multiplicities than the consequent derivation of physical results which are published elsewhere. With reference to a first series of experiments at FOBOS, several applications of this spectrometer are briefly treated.

### 6.1 Fragment spectroscopy of spontaneous fission

Considerable progress in detection techniques for FF has been achieved in recent years, and high resolution data have been obtained for spontaneous fissioning nuclides. With the help of a twin ionization chamber (E-E-method [47]) single FF masses could be resolved in the cold fission region [48]. This method loses its outstanding performance for lower total kinetic energies (TKE) of the FF because neutron emission affects the measured energies. (Every emitted neutron additionally deteriorates the mass determination of the FF by approximately  $\sigma_m \approx 1.5$  a.m.u. due to the recoil. Furthermore, prior-to-fission and post-fission neutron emission quantities are mixed in the analysis.)

Correlation measurements for pairs of FF from spontaneous fission have been performed at the FOBOS spectrometer applying the TOF-TOF-method [49]. The START-signal was delivered by either a channel-plate detector or a transmission avalanche counter, and the STOP-signals were generated by the large-area PSAC. By operating several PSAC and correcting the position-dependence of the timing signals, the main drawback of most TOF measurements — their low geometrical efficiency — has been overcome. Although single masses were not resolved in the cold fission region, the TOF-TOF-method provides the following advantages, especially at lower TKE (tab. 3):

- (i) For nuclides with a low fission branch, e.g.  $^{244}\text{Cm(sf)}$  ( $1.5 \cdot 10^6$   $\alpha$ -particles per fission), sufficient statistics of FF coincidences can be easily collected, because the avalanche counters are able to discriminate up to  $10^7$   $\alpha$ -signals per second [50, 51]. At such rates, the E-E-method fails due to the multiple pile-up of  $\alpha$ -particle signals.

- (ii) The FF quantities derived by the TOF-TOF-method are prior-to-neutron-emission ones which are more directly connected with the physics studied in such experiments.
- (iii) The neutron emission affects the mass determination at least two times less than in the case of the E-E-method. Both methods essentially derive the FF mass ratio from the ratio of the measured quantities (eq. 10) assuming momentum conservation.

$$m_1 / m_2 = v_2 / v_1 = e_2 / e_1 \quad (10)$$

A certain relative change of a FF velocity component in flight direction ( $\Delta v_i / v_i$ ) causes a relative change in the FF energy of  $\Delta e_i / e_i = 2 \cdot \Delta v_i / v_i$ .

A further error source of the E-E-method — the dependence of the measured FF energy ratio on the sharing of the neutron emission between both fragments — is absent in the TOF-TOF-method.

A well known problem of charged-particle spectroscopy is the occurrence of tails towards lower energy which are caused by scattering, impact on detector and constructional edges etc. This leads to a background of “wrong” events with too low TKE. A considerable reduction of such a background has been achieved by combining the TOF-TOF-analysis with the independent fragment mass determination from tof and  $e_R$  (see chapter 5). Since in most of the distorted events only one fragment is affected, the sum of the linear momenta of both the FF deviates from zero. Therefore, the result obtained by the TOF-TOF-analysis differs from that based on tof and  $e_R$ . The event was ruled out, if the momentum sum derived from tof and

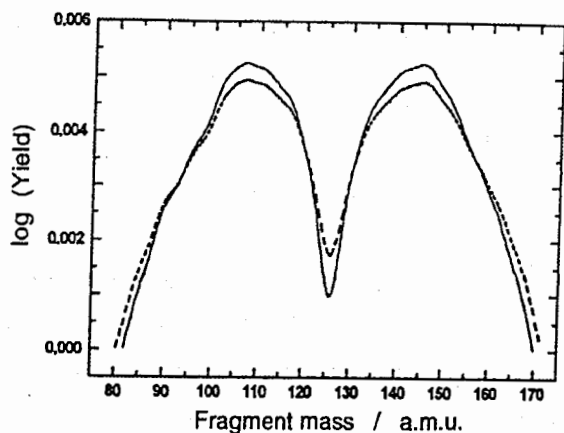


Fig. 35 Mass distribution of fission fragments of a  $^{252}\text{Cf}(sf)$  source as has been measured by use of the TOF-TOF-method. (dashed line: all events; full line: selected events, see text).

$e_R$  was larger than the experimental resolution ( $\Delta p \approx \pm 200 \text{ MeV}/c$ ), or if the difference of both results exceeds their uncertainties. With the help of such a check for consistency, the background at low TKE mentioned above can be suppressed (fig. 35). A value for the peak-to-valley ratio of 52 has been achieved in the FF mass distribution of  $^{252}\text{Cf}(sf)$  [52].

## 6.2 Fragmentation of hot nuclei

### 6.2.1 TKE - M distributions of binary fission of hot nuclei

The TKE of the fragments is a measure of the Coulomb repulsion in the exit channel. It is closely connected with the geometrical and other conditions in a late state of the disintegration process. Since these conditions may change at high temperatures, one is interested in precise TKE-M data for the fission of hot nuclei.

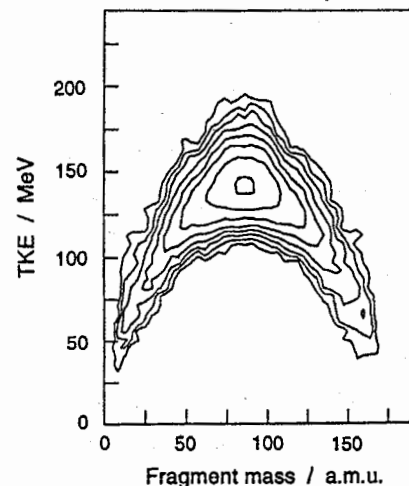


Fig. 36 TKE-M distribution of fragment pairs emitted in the reaction  $^{14}\text{N}$  (34 AMeV) +  $^{197}\text{Au}$  at large linear momentum transfer.

The well known classical tools, e.g. the kinematical coincidence method [53] which utilizes certain kinematical boundary conditions to derive the interesting quantities from the measured velocity vectors of the fragments, involve increasingly larger uncertainties, if the bombarding energy is increased. The reason is, that the

c.m. frame of the fragments in the output channel deviates more and more from the c.m. frame in the input channel due to the fluctuating incomplete momentum transfer in the early stage of reaction and due to fluctuations in the cascade of light-particle evaporation.

The additional information delivered by the FOBOS modules — both fragment masses at scission are determined independently from each other — allows to derive both the TKE and the velocity vectors in the frame of the fissioning system. In this way, any processes which happened before scission do not affect the measured TKE-M distributions. Reconstructing the total transferred linear momentum (LMT) from the parameters  $p_i$  of all fragments in the

collision and applying the massive transfer model [54], the excitation energy ( $E^*$ ) of the decaying system can be evaluated [55, 56]. Furthermore, the low registration thresholds of FOBOS allow to measure TKE-M distributions in a wide range of the fragment mass and to study their dependence on the LMT.

The TKE-M distribution for pairs of fragments emitted in the reaction  $^{14}\text{N}$  (34 AMeV) +  $^{197}\text{Au}$  at large LMT is shown in fig. 36. It is characterized by a large amount of symmetric fission and branches extending to very asymmetric mass splits. The mean TKE in dependence on the mass-asymmetry parameter has been derived. Conclusions about energy dissipation and some confirmation of early theoretical predictions about an unique decay mechanism are given in ref. [57].

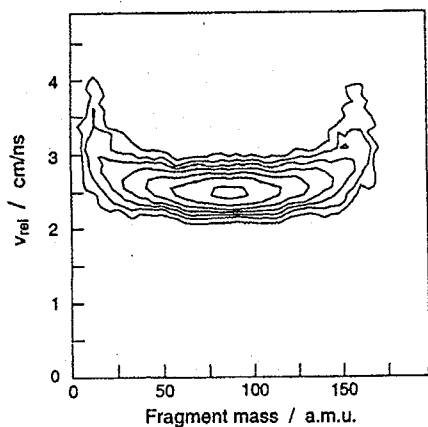


Fig. 37 Relative c.m. velocities ( $v_{\text{rel}}$ ) between binary fragments emitted in the reaction  $^{14}\text{N}$  (34 AMeV) +  $^{197}\text{Au}$ .

The relative c. m. velocities ( $v_{\text{rel}}$ ) between binary fragments from the reaction  $^{14}\text{N}$  (34 AMeV) +  $^{197}\text{Au}$  are given in fig. 37 in dependence on the mass number of one of the partners. The mean values for nearly symmetric disintegrations are in accordance with the systematics of ref. [58].

Deviations from a fission-like behavior have been observed for very asymmetric binary decays. The larger  $v_{\text{rel}}$  should be connected with a more compact configuration at scission [57].

### 6.2.2 Velocity analysis of ternary decays

Hot nuclei with  $E^* \leq 280$  MeV have been produced in the reaction  $^7\text{Li}$  (43 AMeV) +  $^{232}\text{Th}$  [59]. On a yield level of  $\approx 0.1\%$ , the dominating fission channel is competed with IMF-accompanied fission ( $Z_{\text{IMF}} = 3 \div 8$ ) [60, 61], as has already been observed in ref. [62]. The third companion in fission can also be an  $\alpha$ -particle [63].

The independent measurement of the fragment parameters in a  $4\pi$ -geometry enables a velocity analysis with respect to the c. m. of the fissioning system. From both, FF masses and velocities, the frame of the fissioning system was derived, and the velocity of the third fragment

has been transformed into this frame. Two groups of particles with velocities above

$v_{\text{rel}} = 2.5$  cm ns $^{-1}$  and below  $v_{\text{rel}} = 2.4$  cm ns $^{-1}$ , respectively, are clearly distinguished in the reaction  $^{14}\text{N}$  (34 AMeV) +  $^{197}\text{Au}$  (fig. 38).

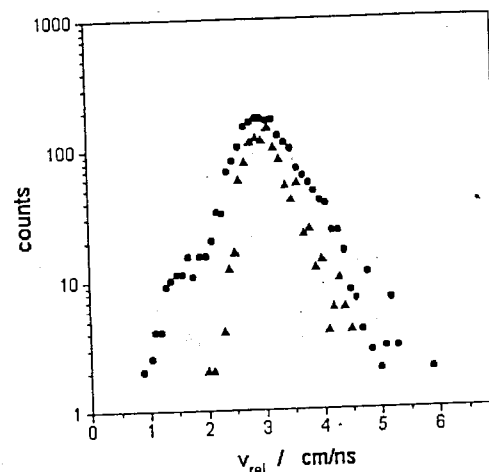


Fig. 38 Relative velocity ( $v_{\text{rel}}$ ) distribution of fragments from binary and ternary decays of the composite system created in the reaction  $^{14}\text{N}$  (34 AMeV) +  $^{197}\text{Au}$ . (full triangles:  $v_{\text{rel}}$  between fragment pairs in very asymmetric binary decays; full circles:  $v_{\text{rel}}$  between the IMF accompanying fission and the c.m. of the fissioning system in ternary decays)

The different dependence on  $E^*$  of the yields of these two components [64] allows to conclude that the high-energy component results from the emission of a hot compound-like nucleus, and the low-energy component arises from an emission during a later stage of the fission process near scission, where the system has a very deformed shape [65].

### 6.2.3 The charged-particle clock

Since the gas-filled detectors of FOBOS are not sensitive to LCP, correlations of fragments with LCP can be investigated within a  $4\pi$ -geometry. Interesting possibilities are opened by the use of LCP as a charged-particle clock for fission of hot nuclei [63, 66].

The principle of the adequate so-called neutron clock is described in ref. [67]. It is based on the discrimination of prior-to-scission- and post-scission-emitted neutron yields which are connected with the time development of the fission process and the corresponding loss of  $E^*$  of the hot nucleus. Conclusions can be made on the dynamics of the fission process [68, 69].

At temperatures of the composite system higher than  $T \approx 3$  MeV, LCP compete with neutrons in the evaporation cascade [70]. Although the neutron multiplicity is larger than the LCP multiplicity, LCP are usually registered with a larger efficiency.

The effective solid angle of the scintillator shell of FOBOS ( $\Delta\Omega_{\text{csl}} \approx 4$  sr) allows coincidence measurements with a high statistical accuracy for the study of the interplay of



fission and LCP emission of hot nuclei. Correlations of LCP with FF have been analyzed for the reaction  $^{14}\text{N}$  (53 AMeV) +  $^{197}\text{Au}$  [60] to distinguish between different sources of LCP emission. The post-scission-emitted component of  $\alpha$ -particles could be separated from the prior-to-scission-emitted one by comparison of the spectra measured at different angles between the main fission axis and the direction of  $\alpha$ -particle emission. Under certain kinematical conditions the post-scission-emitted component occurs at a larger mean energy than the prior-to-scission-emitted one (fig. 39).

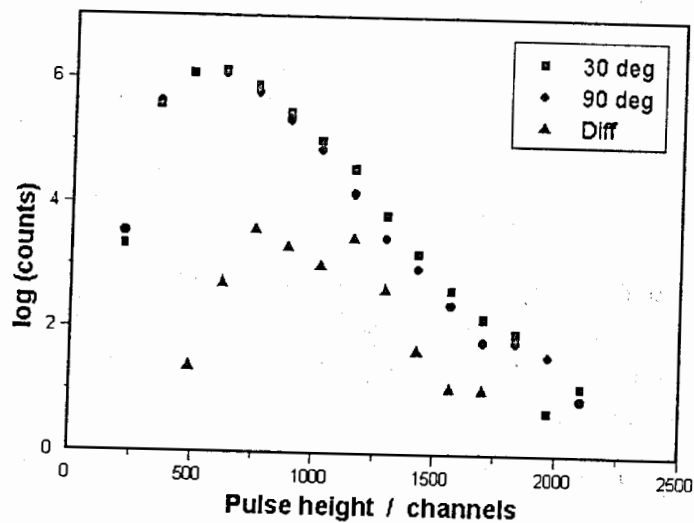


Fig. 39 The post-scission-emitted component of  $\alpha$ -particles (full triangles) has been separated from the prior-to-scission-emitted one by a correlation analysis of the  $\alpha$ -accompanied fission in the reaction  $^{14}\text{N}$  (53 AMeV) +  $^{197}\text{Au}$ . The spectra of  $\alpha$ -particles emitted at a mean angle of  $30^\circ$  and  $90^\circ$  with respect to the fission axis are indicated by full squares and full circles, respectively.

The FOBOS spectrometer provides the means for a detailed study of, e.g., the dependence of the LCP components on the mass asymmetry of the disintegration, promising new insights on the dynamics of the fission process at large primary  $E^*$ .

## 7. SUMMARY

The design, main measuring principles, detectors and service technique of the  $4\pi$ -fragment-spectrometer FOBOS have been described.

Especially attention has been paid to a detailed description of the calibration procedures developed, and to the derivation of physical observables from the measured values. The independent determination of the fragment parameters without any assumptions about the kinematics of the nuclear reaction considered plays a key-role for the investigation of the decay of hot nuclear systems produced by incomplete fusion.

The low registration thresholds and the broad dynamic range of the spectrometer make it a suitable tool for correlation measurements of charged reaction products in the Fermi-energy domain where low fragment multiplicities dominate.

The applied method of measurement has special advantages for the study of spontaneous fission.

## Acknowledgments

It is our want to thank all the people who supported and helped us during the phase of design and construction of the FOBOS spectrometer, who stimulated the development of this device in innumerable useful discussions, who made the first series of experiment proposals, and, last but not least, who gave us technical assistance in solving the well-known everyday problems.

Vicariously for all of them, we wish to thank E.A. Cherepanov, G.G. Chubarian, B. Danziger, J. Fiedler, R. Förster, H. Freiesleben, H. Fuchs, F. Gleisberg, A. Gobbi, E. Grosse, H. Hartwig, D. Hilscher, J. Holik, J. Hutsch, G.F. Issayev, A.I. Ivanenko, W. Janczur, K.-H. Kaun, T. Kiehne, R. Kotte, J. Krüger, A.N. Mezentsev, E. Norbeck, H. Oeschler, J. Peter, H. Prade, M. Renz, A.V. Reshetov, G. Röpke, H. Schopper, H. Schunk, R.H. Siemssen, E.M. Smirnova, M. Sobiella, F. Stary, M. Di Toro, Ts.D. Vylov, D. Walzog, Th. Wilpert, D. Wohlfarth, R. Wolski, V.I. Zagrebaev, and Sh. S. Zeinalov.

We are indebted to the staff of the U-400M cyclotron of the FLNR Dubna for the outstanding co-operation during the experiments, especially to B.N. Gikal, G.G. Gulbekian, and V.B. Kutner.

The careful reading of the manuscript by R. Yanets is gratefully acknowledged.

## Tables

Table 1 : Geometry of the FOBOS spectrometer in its normal position.

Ring	Module type	$\langle \vartheta \rangle$	Module $\langle \varphi \rangle$ Nr.:				
exit	pentagon	0°					
1	hexagon	37.377°	1 : 90°	2 : 162°	3 : 234°	4 : 306°	5 : 18°
2	pentagon	63.435°	6 : 126°	7 : 198°	8 : 270°	9 : 342°	10: 54°
3	hexagon	79.187°	11: 90°	12: 162°	13: 234°	14: 306°	15: 18°
4	hexagon	100.813°	16: 126°	17: 198°	18: 270°	19: 342°	20: 54°
5	pentagon	116.565°	21: 90°	22: 162°	23: 234°	24: 306°	25: 18°
6	hexagon	142.623°	26: 126°	27: 198°	28: 270°	29: 342°	30: 54°
entrance	pentagon	180°					

Table 2 : Geometry of the FOBOS forward array.

Ring	Number of phoswich detectors	$\langle \vartheta \rangle$
1	12	5°
2	16	8°
3	16	10.5°
4	16	14°
5	16	18.5°
6	16	23.5°

Table 3 : Uncertainties ( $1\sigma$  / a.m.u.) of the fragment mass determination for different neutron multiplicities.

Method	$\sigma_m(0n)$	$\sigma_m(1n)$	$\sigma_m(4n)$
E - E	$< 0.2^1$	1.5 <sup>3</sup>	3.5 <sup>3</sup>
TOF-TOF	0.4 <sup>2</sup>	0.7 <sup>3</sup>	1.4 <sup>3</sup>

<sup>1</sup> from cold fission spectra of ref. [48].

<sup>2</sup> from <sup>252</sup>Cf(sf) data taken at FOBOS [52].

<sup>3</sup> estimated value assuming a neutron kinetic energy of 2 MeV.

## References

- [1] H.-G. Ortlepp, M. Andrassy, G.G. Chubarian, M. Danziger, T. Dietterle, A.S. Fomichev, Sh.M. Heinitz, C.-M. Herbach, A.I. Ivanenko, I.V. Kolesov, D. May, Yu.Ts. Oganessian, Yu.E. Penionzhkevich, G. Renz, L.A. Rubinskaya, O.V. Strelalovsky, V.M. Vasko, W.D. Fromm, K. Heidel, H. Sodan, W. Wagner, B.A. Burova, S.V. Radnev, and I.D. Sandrev, Proc. of the Internat. Conf. on New Nuclear Physics with Advanced Techniques, Ierapetra, Crete, Greece, 1991 (Eds. F.A. Beck, S. Kossionides & C.A. Kalfas) World Scientific, Singapore, 1992, p. 302;  
Proc. of the Internat. Conf. on Exotic Nuclei, Foros, Crimea, Ukraine, 1991 (Eds. Yu.E. Penionzhkevich and R. Kalpakchieva) World Scientific, Singapore, 1992, p. 345.
- [2] H.-G. Ortlepp, M. Andrassy, G.G. Chubarian, M. Danziger, P. Gippner, L. Dietterle, A.S. Fomichev, C.-M. Herbach, A.I. Ivanenko, I.V. Kolesov, A. Matthies, D. May, Yu.Ts. Oganessian, Yu.E. Penionzhkevich, V.N. Pokrovsky, G. Renz, L.A. Rubinskaya, O.V. Strelalovsky, V.V. Trofimov, V.M. Vasko, K. Heidel, K.D. Schilling, W. Seidel, H. Sodan, W. Wagner, V.E. Zhuchko, H. Fuchs, D. Hilscher, H. Homeyer, P. Ziem, G. Pausch, B.A. Burova, S.V. Radnev, and I.D. Sandrev, Proc. of the Internat. School-Seminar on Heavy Ion Physics, Dubna, Russia, 1993 (Eds. Yu.Ts. Oganessian, Yu.E. Penionzhkevich, and R. Kalpakchieva) JINR E7-93-247, Dubna, 1993, vol. 2, p. 466;  
Proc. of the FOBOS workshop '94, Cracow, Poland, 1994 (Ed. W. Wagner) FZR-65, Rossendorf, Germany, 1995, p. 29;  
M. Andrassy, A.A. Aleksandrov, I.A. Aleksandrova, A. Budzanowski, M. Danziger, L. Dietterle, V.N. Doronin, S. Dshemuchadse, A.S. Fomichev, P. Gippner, M. Gebhardt, K. Heidel, Sh. Heinitz, C.-M. Herbach, D. Hilscher, J. Holik, H. Homeyer, A.I. Ivanenko, S.A. Ivanovsky, W. Janczur, D.V. Kamanin, I.V. Kolesov, A. Matthies, D. May, S.I. Merzlyakov, W. von Oertzen, Yu.Ts. Oganessian, H.-G. Ortlepp, G. Pausch, Yu.E. Penionzhkevich, V.N. Pokrovsky, Yu.V. Pyatkov, S.V. Radnev, G. Renz, L.A. Rubinskaya, I.D. Sandrev, K.D. Schilling, W. Seidel, D.I. Shishkin, H. Sodan, O.V. Strelalovsky, V.V. Trofimov, I.P. Tsurin, C. Umlauf, D.V. Vakotov, V.M. Vasko, W. Wagner, V.E. Zhuchko, P. Ziem, and L. Zrodowski, JINR E7-95-148, Dubna, Russia, 1995.
- [3] E. Will, H. Sodan, I.V. Kolesov, R. Kupchak, Yu.E. Penionzhkevich, Yu.Ts. Oganessian, and W. Seidel, Contr. at the Symp. on Experiments on Heavy Ion Beams, Varna, Bulgaria, 1984, JINR D7-84-736, Dubna, 1984, p. 70;  
H. Sodan, I.V. Kolesov, Yu.Ts. Oganessian, Yu.E. Penionzhkevich, D. Walzog, W. Seidel, R. Kotte, H.-G. Ortlepp, F. Stary, B.A. Burova, R.G. Kalpakchieva, S.V. Radnev, and I.V. Sandrev, Proc. of the Internat. School-Seminar on Heavy Ion Physics, JINR Dubna, 1986;  
A.G. Akhperdzanian, B.A. Burova, D. Walzog, W. Seidel, H. Sodan, R.G. Kalpakchieva, I.V. Kolesov, R. Kotte, Yu.Ts. Oganessian, H.-G. Ortlepp, Yu.E. Penionzhkevich, S.V. Radnev, I.D. Sandrev, F. Stary, A.S. Fomichev, and G.G. Chubarian, JINR P13-87-760, Dubna, 1987.
- [4] G.N. Flerov, Yu.Ts. Oganessian, S.L. Bogomolov, B.N. Gikal, G.G. Gulbekian, A.I. Ivanenko, V.V. Kamanin, B.A. Klenin, S.I. Kozlov, I.V. Kolesov, V.B. Kutner, V.N. Melnikov, E.A. Minin, A.M. Morduyev, P.Ts. Oganessian, A.S. Pasyuk, Yu.E. Penionzhkevich, K.I. Semin, B.V. Fefilov, and V.A. Chugreev, JINR 9-84-555, Dubna, 1984.
- [5] S. Biri, A.A. Efremov, and V.B. Kutner, in: "Heavy Ion Physics", Scientific Report 1989/90 (Ed. B.I. Pustylnik) JINR E7-91-75, Dubna, Russia, 1991, p. 208.
- [6] Yu.Ts. Oganessian and Yu.E. Penionzhkevich, JINR E7-94-245, Dubna, Russia, 1994.
- [7] W. Wagner, A.S. Fomichev, C.-M. Herbach, A. Matthies, H.-G. Ortlepp, G. Pausch, O.V. Strelalovsky, and V.A. Vitenko, in: "Heavy Ion Physics", Scientific Report 1991/92 (Ed. B.I. Pustylnik) JINR E7-93-57, Dubna, Russia, 1993, p. 244;  
W. Wagner, A.S. Fomichev, H.-G. Ortlepp, C.-M. Herbach, A. Matthies, G. Pausch, O.V. Strelalovsky, M.A. Milovidov, and V.A. Vitenko, JINR Rapid Comm. 4 [61]-93, Dubna, Russia, 1993, p. 49;  
W. Wagner, H.-G. Ortlepp, D.V. Kamanin, A. Matthies, O.V. Strelalovsky, and V.E. Zuchko, Proc. of the FOBOS workshop '94, Cracow, Poland, 1994 (Ed. W. Wagner) FZR-65, Rossendorf, Germany, 1995, p. 40;

- A.S. Fomichev, H.-G. Ortlepp, Yu.E. Penionzhkevich, C.-M. Herbach, I. David, W. Wagner, G. Pausch, H. Sodan, and V.A. Vitenko, JINR P15-92-50, Dubna, Russia, 1992.
- [8] A.A. Aleksandrov, I.A. Aleksandrova, M. Andrassy, W. Wagner, P. Gippner, S. Dshemuchadse, G. Pausch, D.V. Kamanin, A. Matthies, H.-G. Ortlepp, and O.V. Strelalovsky, Pribory i Technika Eksperimenta, Nr. 6, 1996, p. 1. (in Russian)
- [9] G.D. Westfall, J.E. Yurkon, G. Van der Plicht, Z.M. Koenig, B.V. Jacak, R. Fox, G.M. Crawley, M.R. Maier, B.E. Hasselquist, R.S. Tickle, and D. Horn, Nucl. Instr. and Meth. A238 (1985) 347.
- [10] S.V. Radnev, I.D. Sandrev, B.D. Burova, Ch.K. Patchadshiev, Ts.R. Predov, and S.G. Gentchev, Contr. at the Internat. Conf. on Set-up FOBOS, Sofia, Bulgaria, 1990, JINR D7-90-539, Dubna, Russia, 1990, p. 17.
- [11] W. Seidel, H.-G. Ortlepp, F. Stary, and H. Sodan, Nucl. Instr. and Meth. A273 (1988) 536.
- [12] J. Pouthas, B. Borderie, R. Dayras, E. Plagnol, M.F. Rivet, F. Saint-Laurent, J.C. Steckmeyer, G. Auger, C.O. Bacri, S. Barbey, A. Barbier, A. Benkirane, J. Benlliure, B. Berthier, E. Bougamont, P. Bourgault, P. Box, R. Bzyl, B. Cahan, Y. Cassagnou, D. Charlet, J.L. Charvet, A. Chbihi, T. Clerc, N. Copinet, D. Cussol, M. Engrand, J.M. Gautier, Y. Huguet, O. Jouniaux, J.L. Laville, P. Le Botlan, A. Leconte, R. Legrain, P. Lelong, M. Le Guay, L. Martina, C. Mazur, P. Mosrin, L. Olivier, J.P. Passerieux, S. Pierre, B. Piquet, E. Plaige, E.C. Pollacco, B. Raine, A. Richard, J. Ropert, C. Spitaels, L. Stab, D. Sznajderman, L. Tassan-got, J. Tillier, M. Tripon, P. Vallerand, C. Volant, P. Volkov, J.P. Wieleczo, and G. Wittwer, Nucl. Instr. and Meth. A357 (1995) 418.
- [13] C.R. Grun, M. Bimini, R. Legrain, R. Loveman, W. Pang, M. Roach, D.K. Scott, A. Shotter, T.J. Symons, J. Wouters, M. Zisman, R. de Vries, Y.C. Peng, and W. Sondersheim, Nucl. Instr. and Meth. 196 (1982) 33.
- [14] A. Matthies, W. Seidel, R. Kotte, and H.-G. Ortlepp, Contr. at the Symp. on Correlation Experiments on Heavy Ion Beams, Dresden, 1988, JINR D7-88-299, Dubna, 1988, p. 11.

- [15] O. Buneman, T.E. Granshaw, and J.A. Harvey, Can. Journ. Res. A27 (1949) 191.
- [16] H.-G. Ortlepp and A. Romaquera, Nucl. Instr. and Meth. A267 (1989) 500.
- [17] A.A. Aleksandrov, I.A. Aleksandrova, L. Dietterle, V.N. Doronin, S. Dshemuchadse, P. Gippner, C.-M. Herbach, S.A. Ivanovsky, D.V. Kamanin, A. Matthies, D. May, H.-G. Ortlepp, G. Pausch, Yu.E. Penionzhkevich, G. Renz, K.D. Schilling, D.I. Shishkin, O.V. Strelalovsky, V.V. Trofimov, I.P. Tsurin, C. Umlauf, D.V. Vakotov, V.M. Vasko, W. Wagner, and V.E. Zhuchko, in: "Heavy Ion Physics", Scientific Report 1993/94 (Ed. B.I. Pustyl'nik) JINR E7-95-227, Dubna, Russia, 1995, p. 211.
- [18] G. Renz, E. Will, W. Seidel, D. Walzog, and H.-G. Ortlepp, Contr. at the Symp. on Correlation Experiments on Heavy Ion Beams, Dresden, 1988, JINR D7-88-299, Dubna, 1988, p. 17.
- [19] G. Renz, V.M. Vasko, P. Gippner, A. Matthies, V.N. Doronin, D.I. Shishkin, C. Umlauf, and M. Gebhardt, Proc. of the FOBOS workshop '94, Cracow, Poland, 1994 (Ed. W. Wagner) FZR-65, Rossendorf, Germany, 1995, p. 46; G. Renz, V.M. Vasko, P. Gippner, A. Matthies, V.N. Doronin, D.I. Shishkin, C. Umlauf, and M. Gebhardt, FZR-78, Rossendorf, Germany, 1995, p. 115; G. Renz, V.M. Vasko, P. Gippner, A. Matthies, V.N. Doronin, D.I. Shishkin, C. Umlauf, and M. Gebhardt, in: "Heavy Ion Physics", Scientific Report 1993/94 (Ed. B.I. Pustyl'nik) INR E7-95-227, Dubna, Russia, 1995, p. 222.
- [20] M. Gebhardt, Diploma Thesis, Johann Wolfgang Goethe - Universität, Frankfurt am Main, Germany, 1995; M. Gebhardt, V.N. Doronin, P. Gippner, H.-G. Ortlepp, G. Renz, D.I. Shishkin, and W. Wagner, FZR-78, Rossendorf, Germany, 1995, p. 81.
- [21] O.V. Strelalovsky, K. Heidel, S.I. Ivanovsky, D. May, H.-G. Ortlepp, G. Pausch, G. Renz, V.E. Zhuchko, W. Wagner, V.V. Trofimov, and I.P. Tsurin, Proc. of the XVI Internat. Symp. on Nuclear Electronics and VI Internat. School on Automation and Computing in Nuclear Physics and Astrophysics, Varna, Bulgaria, 1994 (Ed. I.N. Churin) JINR D13-94-491, Dubna, Russia, 1995, p. 31;

- O.V. Strelakovsky, K. Heidel, S.I. Ivanovsky, D. May, H.-G. Ortlepp, G. Pausch, G. Renz, V.V. Trofimov, I.P. Tsurin, W. Wagner, and V.E. Zhuchko, Proc. of the FOBOS workshop '94, Cracow, Poland, 1994 (Ed. W. Wagner) FZR-65, Rossendorf, Germany, 1995, p. 49.
- [22] J. Alarja, A. Dauchy, A. Giorni, C. Morand, E. Pollaco, P. Stassi, R. Billerey, B. Chambon, B. Cheynis, D. Drain, and C. Pastor, Nucl. Instr. and Meth. A 242 (1986) 352.
- [23] F. Benrachi, B. Chambon, B. Cheynis, D. Drain, C. Pastor, D. Seghier, K. Zaid, A. Giorni, D. Heuer, A. Llères, C. Morand, P. Stassi, and J.B. Viano, Nucl. Instr. and Meth. A281 (1989) 137.
- [24] W. Terlau, PhD Thesis, Freie Universität Berlin, Germany, 1988.
- [25] J. Töke, S.A. Masserant, S.P. Baldwin, B. Lott, W.U. Schröder, and X. Zhao, UR-NSRL-394, University of Rochester, USA, 1993.
- [26] P. Ziem, T. Kiehne, L. Dietterle, and V.V. Trofimov, FZR-92-11, Rossendorf, Germany, 1992, p. 19.
- [27] STRUCK - Product Summary, Hamburg, Germany, 1990.
- [28] C.A.E.N. - General Catalogue, Viareggio, Italy, 1993.
- [29] LeCroy - Research Instrumentation Catalog, Chestnut Ridge NY, USA, 1992.
- [30] C.-M. Herbach and C. Umlauf, in: "Heavy Ion Physics", Scientific Report 1991/92, (Ed. B.I. Pustyl'nik) JINR E7-93-57, Dubna, Russia, 1993, p.250.
- [31] G. Röscher, HMI-B436, Berlin, Germany, 1986; G. Röscher, "HOOPSY under VMS - A Program System for Multi-Parameter-Experiments", Version 12, Hahn-Meitner-Institut, Berlin, Germany, 1992.
- [32] K.-P. Eckert, S. Gipp, and S. Wasserroth, HMI-D/M 154, Berlin, Germany, 1984; "OLYMP - A System for the Evaluation of multi- dimensional experimental Data and Spectra", Version 5.4, Hahn-Meitner-Institut, Berlin, Germany, 1992.
- [33] C.-M. Herbach and D.V. Vakarov, Proc. of the FOBOS workshop '94, Cracow, Poland, 1994 (Ed. W. Wagner) FZR-65, Rossendorf, Germany, 1995, p. 56.

- [34] B. Stroustrup, "The C++ Programming Language", Addison-Wesley, 1986.
- [35] D.A. Young, "Object-Oriented Programming with C++ and OSF / MOTIF", Prentice Hall, 1992.
- [36] M.I. Belyakov, Yu.I. Rabover, and A.L. Fridman, "The Portable Operational System", Radio i Svyaz, Moscow, Russia, 1991. (in Russian)
- [37] H. Stelzer, "CAMDA - a CAMAC-PC Data Acquisition System", Messel, Germany, 1989.
- [38] Ch. Schulz, Diploma Thesis, Technische Universität Berlin, Germany, 1995.
- [39] J. Henninger and B. Horlbeck, JINR E6-84-366, Dubna, Russia, 1984.
- [40] W. Wagner and D.V. Kamanin, FZR-130, Rossendorf, Germany, 1996, p. 150.
- [41] D. Horn, G.C. Ball, A. Galindo-Uribarri, E. Hagberg, R.B. Walker, R. Laforest, and J. Pouliot, Nucl. Instr. and Meth. A320 (1992) 273; A.S. Fomichev, I. David, S.M. Lukyanov, Yu.E. Penionzhkevich, N.K. Skobelev, O.B. Tarasov, A. Matthies, H.-G. Ortlepp, W. Wagner, M. Lewitowicz, M.G. Saint-Laurent, J.M. Corre, Z. Dlouhy, I. Pecina, and C. Borcea, Nucl. Instr. and Meth. A344 (1994) 378.
- [42] S. Kahlbitzer, H. Oetzmann, H. Grahmann, and A. Feuerstein, Z. Phys. A278 (1976) 233.
- [43] C.-M. Herbach and H.-G. Ortlepp, in: "Heavy Ion Physics", Scientific Report 1991/92 (Ed. B.I. Pustyl'nik) JINR E7-93-57, Dubna, Russia, 1993, p. 253.
- [44] J.F. Ziegler, "Handbook of Stopping Cross-Sections for Energetic Ions in All Elements", Pergamon Press, New York, 1980.
- [45] J.H. Ormrod, J.R. Macdonald, and H.E. Duckworth, Can. Journ. Phys. 43 (1965) 275.
- [46] R. Schmidt and H. Henschel, Nucl. Phys. A395 (1983) 15.
- [47] C. Budtz-Jørgensen, H.-H. Knitter, Ch. Straede, F.-J. Hamsch, and R. Vogt, Nucl. Instr. and Meth. A258 (1987) 209.
- [48] H.-H. Knitter, F.-J. Hamsch, and C. Budtz-Jørgensen, Nucl. Phys. A536 (1992) 221.

- [49] Yu.V. Pyatkov, A.A. Aleksandrov, I.A. Aleksandrova, B.I. Andreev, P. Gippner, C.-M. Herbach, E.M. Kozulin, A. Matthies, Yu.Ts. Oganessian, H.-G. Ortlepp, Yu.E. Penionzhkevich, G. Renz, K.D. Schilling, O.V. Strelakovsky, V.M. Vasko, and W. Wagner, Proc of the Internat. Workshop on Nuclear Fission and Fission Product Spectroscopy, Château de la Baume, Seyssins, France, 1994 (Eds. H. Faust & G. Fioni) Grenoble, 1994, p. 144.
- [50] Yu.V. Pyatkov, A.A. Aleksandrov, B.I. Andreev, P. Gippner, C.-M. Herbach, H.-G. Ortlepp, Yu.E. Penionzhkevich, R.A. Shekhmamet'ev, and W. Wagner, FZR-98, Rossendorf, Germany, 1995.
- [51] A.A. Aleksandrov, B.I. Andreev, P. Gippner, C.-M. Herbach, E.M. Kozulin, A. Matthies, Yu.Ts. Oganessian, H.-G. Ortlepp, Yu.E. Penionzhkevich, Yu.V. Pyatkov, G. Renz, K.D. Schilling, O.V. Strelakovsky, V.M. Vasko, and W. Wagner, FZR-99, Rossendorf, Germany, 1995.
- [52] Yu.V. Pyatkov, V.V. Pashkevich, Yu.E. Penionzhkevich, V.G. Tishchenko, A.V. Unzhakova, H.-G. Ortlepp, P. Gippner, C.-M. Herbach, and W. Wagner, Proc. of the 3<sup>d</sup> Internat. Conf. on Dynamical Aspects of Nuclear Fission, Casta-Papiernicka, Slovak Republic, 1996. (in print)
- [53] A. Gobbi and W. Nörenberg, in: "Heavy Ion Collisions" (Ed. R. Bock) North-Holland, Amsterdam, 1980, vol. 2, p. 128; W.U. Schroeder and J.R. Huizenga, in: "Treatise on Heavy-ion Science" (Ed. D.A. Bromley) Plenum Press, New York, 1984, vol. 2, p. 115; G. Casini, P.R. Maurenzig, A. Olmi, and A.A. Stefanini, Nucl. Instr. and Meth. A277 (1989) 445.
- [54] D. Guerreau, GANIL P89-07, Caen, France, 1989; L.G. Moretto and G.J. Wozniak, in: "Progress in Particle and Nuclear Physics" (Ed. A. Faessler) Pergamon Press, New York, 1988, vol. 21, p. 401.
- [55] C.-M. Herbach, Proc. of the FOBOS workshop '94, Cracow, Poland, 1994 (Ed. W. Wagner) FZR-65, Rossendorf, Germany, 1995, p. 87.

- [56] H.-G. Ortlepp, W. Wagner, A.A. Aleksandrov, I.A. Aleksandrova, L. Dietterle, V.N. Doronin, P. Gippner, C.-M. Herbach, S.A. Ivanovsky, D.V. Kamanin, A. Matthies, G. Pausch, Yu.E. Penionzhkevich, G. Renz, K.D. Schilling, D.I. Shishkin, O.V. Strelakovsky, V.V. Trofimov, I.P. Tsurin, C. Umlauf, D.V. Vakarov, V.M. Vasko, and V.E. Zhuchko, in: "Low Energy Nuclear Dynamics" (Eds. Yu. Oganessian, W. von Oertzen, and R. Kalpakchieva) World Scientific, Singapore, 1995, p. 231.
- [57] W. Wagner, H.-G. Ortlepp, P. Gippner, and C.-M. Herbach, in: "Advances in Nuclear Dynamics 2" (Eds. W. Bauer and G.D. Westfall) Plenum Press, New York, 1996, p. 341.
- [58] V.E. Viola, Jr., Nucl. Data- Sect. A1 (1966) 391; V.E. Viola, K. Kwiatkowski, and M. Walker, Phys. Rev. C31 (1985) 1550.
- [59] A.A. Aleksandrov, I.A. Aleksandrova, M. Andrassy, L. Dietterle, V.N. Doronin, P. Gippner, C.-M. Herbach, D. Hilscher, S.A. Ivanovsky, A. Matthies, D. May, H.-G. Ortlepp, G. Pausch, Yu.E. Penionzhkevich, V.N. Pokrovsky, G. Renz, K.D. Schilling, D.I. Shishkin, O.V. Strelakovsky, V.V. Trofimov, C. Umlauf, V.M. Vasko, D.V. Vakarov, W. Wagner, and V.E. Zhuchko, Nucl. Phys. A583 (1994) 465c.
- [60] W. Wagner, H.-G. Ortlepp, C.-M. Herbach, P. Gippner, D.V. Kamanin, A. Matthies, Yu.E. Penionzhkevich, G. Renz, K.D. Schilling, O.V. Strelakovsky, D.V. Vakarov, and V.E. Zhuchko, Proc. of the 2<sup>d</sup> Internat. Symp. on Heavy Ion Physics and its Applications, Lanzhou, China, 1995 (Eds. Y.X. Luo, G.M. Jin and J.Y. Liu) World Scientific, Singapore, 1996, p. 217; FZR-104, Rossendorf, Germany, 1995.
- [61] W. Wagner, H.-G. Ortlepp, C.-M. Herbach, P. Gippner, A. Matthies, G. Pausch, Yu.E. Penionzhkevich, G. Renz, K.D. Schilling, O.V. Strelakovsky, and V.E. Zhuchko, Contr. to the Internat. Nuclear Physics. Conference, Beijing, China, 1995, China Institute of Atomic Energy, 1995, p. 5.5-7; FZR-105, Rossendorf, Germany, 1995.

- [62] D.E. Fields, K. Kwiatkowski, K.B. Morley, E. Renshaw, J.L. Wile, S.J. Yennello, V.E. Viola, and R.G. Korteling,  
Phys. Rev. Lett. 69 (1992) 3713.
- [63] K. Siwek-Wilczynska, J. Wilczynski, H.K.W. Leegte, R.H. Siemssen, H.W. Wilschut, K. Grotowski, A. Panasiewicz, Z. Sosin, and W. Wieloch,  
Phys. Rev. C48 (1993) 228.
- [64] C.-M. Herbach, H.-G. Ortlepp, P. Gippner, K.D. Schilling, and W. Wagner,  
FZR-130, Rossendorf, Germany, 1996, p. 89.
- [65] C.-M. Herbach, H.-G. Ortlepp, P. Gippner, D.V. Kamanin, Yu.E. Penionzhkevich, G. Renz, K.D. Schilling, O.V. Strelakovsky, V.G. Tichenko, and W. Wagner,  
Proc. of the Internat. Research Workshop - "Heavy Ion Physics at Low, Intermediate and Relativistic Energies Using  $4\pi$  Detectors - 1996", Poiana Brasov, Romania, 1996 (Ed. M. Petrovici) World Scientific, Singapore. (in print)
- [66] J.P. Lestone, J.R. Leigh, J.O. Newton, D.J. Hinde, J.X. Wei, J.X. Chen, S. Elfström, and M. Zielinska-Pfabe, Nucl. Phys. A559 (1993) 277.
- [67] D.J. Hinde, D. Hilscher, H. Rossner, B. Gebauer, M. Lehmann, and M. Wilpert,  
Phys. Rev. C45 (1992) 1229;  
D.J. Hinde, Nucl. Phys. A553 (1993) 255c;  
D. Hilscher and H. Rossner, Ann. Phys. Fr. 22 (1992) 471.
- [68] K. Siwek-Wilczynska, J. Wilczynski, R.H. Siemssen, and H.W. Wilschut,  
Nucl. Phys. A583 (1995) 141.
- [69] D. Hilscher, in: "Low Energy Nuclear Dynamics" (Eds. Yu. Oganessian, W. von Oertzen, and R. Kalpakchieva) World Scientific, Singapore, 1995, p. 169.
- [70] H. Delagrange, C. Gregoire, F. Scheuter, and Y. Abe,  
Z. Phys. A323 (1986) 437.

Received by Publishing Department  
on April 3, 1997.

4 $\pi$ -спектрометр фрагментов ФОБОС

4 $\pi$ -спектрометр фрагментов ФОБОС, разработанный для исследований на пучках тяжелых ионов с энергиями от 10 до 100 АМэВ, введен в эксплуатацию для физических экспериментов в Лаборатории ядерных реакций им. Г.Н.Флерова Объединенного института ядерных исследований.

Основанная на принципе логарифмического детектора, установка ФОБОС может регистрировать заряженные фрагменты от протонов до тяжелых остаточных ядер в широком динамическом диапазоне.

Позиционно-чувствительные лавинные счетчики, брегговские ионизационные камеры и сцинтилляционные детекторы на базе кристаллов CsI(Tl) образуют три детекторные оболочки. Более гранулярная система из фосwich-детекторов используется в качестве переднего детектора под маленькими полярными углами.

Модулярная конфигурация установки ФОБОС удовлетворяет различным требованиям физических экспериментов в области спектрометрии фрагментов ядерных реакций при средних множественностях частиц.

Работа выполнена в Лаборатории ядерных реакций им. Г.Н.Флерова ОИЯИ.

Препринт Объединенного института ядерных исследований. Дубна, 1997

The 4 $\pi$ -Fragment-Spectrometer FOBOS

The 4 $\pi$ -fragment-spectrometer FOBOS developed for heavy-ion research at beam energies of 10  $\div$  100 A MeV has been commissioned for physical experiments at the FLNR of the Joint Institute for Nuclear Research. Based on the logarithmic detector principle, it is able to register charged fragments from protons up to heavy residual nuclei in a large dynamic range. Position-sensitive avalanche counters, axial ionization chambers and CsI(Tl) scintillation detectors are arranged in three concentric detector shells. An array of phoswich detectors is used as a more granular forward detector at narrow polar angles. The modular concept of FOBOS allows for different experimental application in the field of exclusive fragment spectroscopy at medium multiplicities.

The investigation has been performed at the Flerov Laboratory of Nuclear Reactions, JINR.